

Clemson University

TigerPrints

All Dissertations


Dissertations

12-2022

Elucidation of Active Site and Mechanism of Metal Catalysts Supported in NU-1000

Hafeera Shabbir
hshabbi@clemson.edu

Follow this and additional works at: https://tigerprints.clemson.edu/all_dissertations

 Part of the [Catalysis and Reaction Engineering Commons](#), [Computational Chemistry Commons](#), [Computational Engineering Commons](#), [Materials Chemistry Commons](#), and the [Thermodynamics Commons](#)

Recommended Citation

Shabbir, Hafeera, "Elucidation of Active Site and Mechanism of Metal Catalysts Supported in NU-1000" (2022). *All Dissertations*. 3211.

https://tigerprints.clemson.edu/all_dissertations/3211

This Dissertation is brought to you for free and open access by the Dissertations at TigerPrints. It has been accepted for inclusion in All Dissertations by an authorized administrator of TigerPrints. For more information, please contact kokeefe@clemson.edu.

ELUCIDATION OF ACTIVE SITE AND MECHANISM OF METAL CATALYSTS SUPPORTED IN NU-1000

A Dissertation
Presented to
the Graduate School of
Clemson University

In Partial Fulfillment
of the Requirements for the Degree
Doctor of Philosophy
Chemical Engineering

by
Hafeera Shabbir
December 2022

Accepted by:
Dr. Rachel B. Getman, Committee Chair
Dr. Ming Yang
Dr. Christopher L. Kitchens
Dr. Leah B. Casabianca

Abstract

Advances in extraction of shale oil and gas has increased the production of geographically stranded natural gas (primarily consisting of methane (C1) and ethane (C2)) that is burned on site. A potential utilization strategy for shale gas is to convert it into fuel range hydrocarbons by catalytic dehydrogenation followed by oligomerization by direct efficient catalysts. This work focuses on understanding metal cation catalysts supported on metal-organic framework (MOF) NU-1000 that will actively and selectively do this transformation under mild reaction conditions, while remaining stable to deactivation (via metal agglomeration or sintering). I built computational models validated by experimental methods to elucidate the structure-function relationship of catalysts for reactions of small molecules (ethane in this work) in natural gas. Computational techniques and characterization data from experimental collaborations at Argonne National Lab and Northwestern University were used to build kinetic models to learn about mechanism of ethene hydrogenation on M-NU-1000 catalysts (M = Ni, Cu, Zn, Co, Mn, Fe). Hydrogen adsorption and dissociation barrier is identified as the reason for discrepancy between experimental and computational data. Quantum density functional theory (DFT) simulations and microkinetic modeling on an expanded mechanism with multiple hydrogen adsorption and dissociation steps is performed. The model predicted spin state of metal as an important design variable with high spin and low spin metals following different mechanistic pathways

due to different hydrogen adsorption and dissociation energies. This resolved the discrepancies between the model and experiments. The impact of different modeling choices on microkinetic modeling is analyzed by expanding the method to include Molecular Dynamics (MD) simulations and comparing different catalyst models in ethene dimerization reaction on Ni@NU-1000. Adsorption and desorption steps are identified as being more significant for determining rates than the activated steps. In collaboration with Northwestern University and Stonybrook University, polyoxometalate and polysulfidometalate catalysts supported on NU-1000 active for CO oxidation and electrochemical hydrogen evolution reaction are studied. Computationally elucidated structure of these catalysts is validated by experimental methods (XAS, XRD and DRIFTS) and provided the insight that the clusters need to be reduced further to remove the peripheral sulfur atoms to tailor them for more challenging reductive chemistry. Using this information our collaborators synthesized a catalyst with lower sulfur content that was found to be active for acetylene hydrogenation. Overall, this work furthered our understanding of catalyst structure and mechanisms for reductive chemical transformation for shale gas to liquid conversion with insights that are applicable generally to MOF catalysts.

Dedication

I would like to dedicate this work to my family: my parents, Rukhsana and Shabbir, my siblings, Quratulain, Waleed and Aqsa and my husband, Zarak.

Acknowledgments

I would like to express the deepest gratitude and appreciation for my advisor, Dr. Rachel Getman. I learned how to do research from her. Grad school is not easy, but she has been my biggest supporter and mentor in these 4.5 years. She has extensive knowledge and experience that she used to help me solve problems and navigate tricky situations. She trained and groomed me to achieve my highest potential during my PhD. I look to her for inspiration particularly in how she has balanced her personal and professional lives.

Next, I would like to thank my committee members, Dr. Ming Yang, Dr. Christopher Kitchens, Dr. Leah Casabianca from Clemson University and my collaborators, Dr. Joe Hupp, Dr. Subhadip Goswami and Dr. Qin Liu from Northwestern University, Zhihengyu Chen and Dr. Karena Chapaman from Stonybrook Unievrsity, Dr. Magali Ferrandon, Dr. Alex Martenson and Dr Massimiliano Delferro for the excellent discussions and prompt feedback. I would also like to thank my group mates, Dr. Steven Pellizzeri, Dr. Paul Meza-Morales, Dr. Tianjun Xie, Dr. Jiazhou Zhu, Dr. Xiaohong Zhang, Dr. Ali Estejab, Dr. Sanchari Bhattacharjee, and (future PhDs) Stephen Vicchio, Ricardo Garcia, Jiexin Shi, Xiuting Chen, Rohit Punyapu and Sayanai Biswas for valuable discussions and suggestions. Further, I would like to thank Dr. David Bruce, Terri McAllister, Joy Rodatz, Diana Stamey, Caitlin Clark and Bill Coburn, for their support with all of the administrative tasks. Last but not

least, I am grateful for support from the Inorganometallic Catalyst Design Center, an Energy Frontiers Research Center funded by the US Department of Energy (DOE) Office of Science, Basic Energy Sciences (BES) under award DE-SC0012702, and the Cyberinfrastructure Technology Integration Group for the support of computing resources on the Palmetto Cluster at Clemson University.

Table of Contents

Title Page	i
Abstract	ii
Dedication	iv
Acknowledgments	v
List of Tables	ix
List of Figures	x
1 Introduction and Background	1
1.1 Motivation	1
1.2 Metal-Organic Frameworks (MOFs) as Catalysts and Supports	2
1.3 MOF NU-1000	4
1.4 Dissertation Outline	6
2 Methods	7
2.1 Overview of Computational Modeling Techniques in MOFs	7
2.2 Catalyst Models	10
2.3 Simulation Methods	13
3 Microkinetic Modeling of Ethene Hydrogenation on Single-site Cation Catalysts Supported in NU-1000	17
3.1 Introduction	17
3.2 Methods	19
3.3 Results	25
3.4 Discussion	28
3.5 Conclusions	34
4 Structure Elucidation of Polyoxometalate Catalysts supported in NU-1000	35
4.1 Introduction	35

4.2	Experimental Methods and Results	39
4.3	Computational Methods	44
4.4	Results and Discussion	45
4.5	Conclusions	51
5	Analyzing choices in microkinetic modeling	52
5.1	Introduction	52
5.2	Computational Methods	55
5.3	Results and Discussion	57
5.4	Conclusions and Recommendations	65
6	Conclusions and Recommendations	68
6.1	Conclusions	68
6.2	Recommendations	70
	Appendices	73
A	Appendix-A	74
	Bibliography	97

List of Tables

3.1	Mechanism and active site preference for the different spin states considered in this chapter	28
3.2	Calculated H ₂ adsorption free energies on the metal hydride (rxn (2)) versus bare metal cation (rxn (1)) for Mn, Fe, and Co@NU-1000 catalysts in kJ/mol. Endergonic values are bolded	29
3.3	Apparent activation energies Mn, Co, Ni, and Cu@NU-1000 catalysts in kJ/mol	31
4.1	Structural information from experimental data for the CoMo ₆ S ₂₄ @NU1000 catalyst	42
4.2	Scaled IR Frequencies by 0.976 of the computed structures of the [RhMo ₆ O ₂₂ H ₆ (CO) ₂] ¹⁻ and RhMoO ₆ O ₂₂ H ₇ (CO) ₂ with different spin states and the experimental values	45

List of Figures

1.1	MOF UiO-66, which has $Zr_6O_4(OH)_4$ nodes and 1,4- benzene-dicarboxylate (BDC) linkers. (a) $Zr_6O_4(OH)_4$ node. (b) Full crystal structure. Color key: Zr=red, O=blue, C=gray, and H=white. Adapted with permission from J. Am. Chem. Soc. 2008, 130, 42, 13850–13851. Copyright 2008 American Chemical Society	3
1.2	Schematic representation of crystal structure of NU-1000. The metal node is the (a) $Zr_6(\mu_3-OH)_4(\mu_3-O)_4(OH)_4(OH_2)_4$ connected by (b) organic tetratopic 1,3,6,8-tetrakis (p-benzoate) pyrene linkers,(c) the hexagonal and triangular channels along the c direction, and (d) the small pore bridging the ab layers along the c direction. Color key: Zr=cyan, O=red, C= gray, H=white. Adapted with permission from J. Catal, 2017, 354, 278-286. Copyright 2017, Elsevier B.V.	5
2.1	Simulation Box that is also the Unit cell of NU-1000 with lattice constants $a = b = 39.897 \text{ \AA}$, $c = 16.635 \text{ \AA}$, $\alpha = \beta = 90^\circ$, $\gamma = 60^\circ$. Ni =orange Zr=cyan O=red C=gray H=white.	10
2.2	Truncated Zr-node of NU-1000 with installed Metal cations (Fe/ Mn/ Fe/ Co/ Ni/ Cu/ Zn) =orange Zr=cyan O=red C=gray H=white	11
2.3	A Model of sulfided Cobalt Molybdenum Oxide catalysts for HER reaction with Co=blue Mo=purple S=yellow	11
2.4	Two cluster models a) charged and b)uncharged of Rh Molybdenum Oxide catalyst for CO oxidation with Rh=dark teal Mo=purple O=red	12
3.1	The SW mechanism. M = metal cation.	19
3.2	a) The NU-1000 crystal structure with the node circled. b) The catalyst model employed in this chapter. c) Metal hydride active site. d) Bare metal cation active site. Color key: carbon = gray, oxygen = red, hydrogen = white, zirconium = teal, metal cation = orange. In b), c) and d), atoms labeled 1, 2, 3, and 4 represent the different sites where hydrogen species are allowed to bind in the density functional theory calculations	21
3.3	Reaction steps followed by the metal cation catalysts studied in this chapter. Rxn numbers correspond to those in the text. The SW mechanism is highlighted.	23

3.4	Log rates in units of moles of ethene converted per metal cation site per second. (a) Experimentally measured. (b) Rates simulated in microkinetic modeling including only the 5 steps that comprise the SW mechanism. (c) Rates simulated using all 22 steps considered in this chapter.	27
3.5	Log rates in units of moles of ethene converted per metal cation site per second. (a) Experimentally measured. (b) Rates simulated in microkinetic modeling including only the 5 steps that comprise the SW mechanism. (c) Rates simulated using all 22 steps considered in this chapter.	32
4.1	Classical POM structures in polyhedral representations. Adapted with permission from Coord. Chem. Rev, 2015, 286, 17-29, Copyright 2014 Elsevier B.V.	36
4.2	(a) Crystal structure of NU-1000, showing the 3.1 nm and 12 nm channels. Each layer is separated by 1.0 nm windows. The structures for the nodes and linkers are given. Polyhedral representation and size of (b) $[\text{Mo}_7\text{O}_{24}\text{H}_6]^{6-}$ and (c) $[\text{RhMo}_6\text{O}_{24}\text{H}_6]^{3-}$ seen from the top and side and molecular representation and size of (d) $[\text{CoMo}_6\text{O}_{24}\text{H}_6]^{3-}$ and (e) $[\text{CoMo}_6\text{S}_{12}\text{H}_{12}]^{4-}$ seen from the top and side. C= gray, Zr= green, H= white, O= red, Mo= purple, Rh= light green, Co= blue, S= yellow .	38
4.3	DRIFT spectra of CO adsorption on the unsupported $\text{RhMo}_6\text{O}_{24}$ and $\text{RhMo}_6\text{O}_{24}@\text{NU1000}$ catalysts at room temperature. Spectra were collected after CO adsorption to saturation and Ar purging. Catalyst exposed to CO showing two main characteristic CO vibrations.	40
4.4	Experimental dPDF of the $\text{CoMo}_6\text{S}_{24}@\text{NU-1000}$ catalyst from XRD. .	42
4.5	$[\text{RhMo}_6\text{O}_{24}\text{H}_6]^{3-}$ structure. C=gray, H= white, O=red, Mo=purple, Rh=blue	43
4.6	$[\text{Mo}_7\text{O}_{24}]^{6-}$ structure obtained from the CAS database registry Number 126094-83-5	43
4.7	Representation of two catalysts models a) $[\text{RhMo}_6\text{O}_{22}(\text{CO})_2\text{H}_6]^{1-}$ and b) $\text{RhMo}_6\text{O}_{22}(\text{CO})_2\text{H}_7$ with their corresponding IR spectrum from Gaussian-09 C=gray, H= white, O=red, Mo=purple, Rh=blue	46
4.8	Example of structures that are a) uncharged with formula $[\text{CoMo}_6\text{S}_{12}\text{H}_12]^{0}$ with 63% short and 54% long pearson correlation and b) positively charged with formula $[\text{CoMo}_6\text{S}_{24}]^{2+}$ with of 81% short and 65% long pearson correlation c) an oxygen substituted configuration with formula $[\text{CoMo}_6\text{S}_{23}\text{O}]^{0}$ with 81% short and 65% long pearson correlation and d) another oxygen substituted configuration positively charged with formula $[\text{CoMo}_6\text{S}_{23}\text{O}]^{0}$ with 83% short and 66% long pearson correlation. C=gray, H= white, S=yellow, O= red, Mo=purple, Co=blue	48

4.9	a)[CoMo ₆ S ₁₂ H ₁₂] ⁴⁻ with 87.9 % short and 78.4% long pearson correlation C=gray, H= white, S=yellow, Mo=purple, Co=blue	49
4.10	a)[CoMo ₆ S ₁₂ H ₁₂] ⁴⁻ (octet spin state) with 93% short and 80% long pearson correlation b) dpdf of the bond lengths for red = computational structure blue = experimental	50
5.1	Different types of molecule transport in MOFs are determined by host-guest interactions	53
5.2	Cossee-Arlman Mechanism of Ethene dimerization on NU-1000 catalyst	58
5.3	Comparing the difference in rates for the model in the truncated cluster Gaussian 09 (M06-L and PBE functionals) periodic CP2K models . .	59
5.4	Truncated cluster Gaussian 09 (M06-L and PBE functionals) and periodic CP2K models (PBE functional) a) Desorption energies b) forward and backward activation energies with tabulated mean and standard deviation values	60
5.5	Variation in adsorption rate of 100% ethene versus the ethene dimerization rate at T = 300 K, P = 1 atm	62
5.6	Contact frequency of C ₂ H ₄ with Ni versus the Ni to C ₂ H ₄ distances .	62
5.7	Adsorption Isotherms generated from GCMC simulations	63
5.8	AIMD Configurations	66

Chapter 1

Introduction and Background

1.1 Motivation

The United States' transportation sector is dominated by traditional petroleum resources [1] with gasoline accounting for 35% of the projected global transportation fuel consumption in 2040 [2]. Advances in hydraulic fracturing and horizontal drilling have increased the shale oil and gas production. Similar to natural gas, shale gas has methane as the primary component (50% to 90%) followed by other hydrocarbons called natural gas liquids (NGL) that comprise of ethane, propane, butane, isobutane, and pentane [3, 4, 5, 6]. Not all of the produced methane and NGL can be transported to gas processing or upgrading facilities due to insufficient pipeline infrastructure in several remote shale gas basins. One solution is to convert these low value hydrocarbons to high value fuels by gas-to-liquid (GTL) process at the well-head in remote areas by using specialized active and selective catalysts. The conventional method for the GTL process involves the partial oxidation of natural gas to obtain synthetic gas composed of CO and H₂, followed by chain growing processes such as Fischer–Tropsch [7] which is expensive and chemically complex. A possible alternative is to consider the

catalytic dehydrogenation of light alkanes followed by oligomerization of the olefins to form fuel range hydrocarbons by direct efficient catalysts [8].

A grand challenge in catalysis research is ‘designing’ catalysts to convert these light hydrocarbons in shale gas to denser compounds or platform molecules that can be further converted into fuels and chemicals [9, 10]. Ideally, catalysts would exist that could produce such products actively and selectively from shale gas under mild reaction conditions, while remaining stable to deactivation (via metal agglomeration or sintering, for example). Designing such catalysts requires combining active and selective catalytic sites with supports that can maintain catalytic stability. While a variety of catalysts have been used for conversion of light hydrocarbons, metal cation catalysts have been relied upon for decades. For example, homogeneous ligated Ni complexes are well-known to promote ethene oligomerization [11], including being used commercially in the Shell higher oligomers process (SHOP) [12], and heterogeneous NiO, NiSO₄, and Ni exchanged zeolite catalysts are active for ethene oligomerization, even under mild reaction conditions [13]. Further, a variety of homogeneous and heterogeneous metal cation-based catalysts are used industrially for hydrocarbon hydrogenation, dehydrogenation, and transfer hydrogenation reactions [14, 15].

1.2 Metal-Organic Frameworks (MOFs) as Catalysts and Supports

Metal-organic frameworks (MOFs) consist of metal cation-based nodes connected with organic linkers in 3D or 2D porous arrangements (e.g., see figure 1.1 of the MOF UiO-66, which has been studied somewhat extensively for applications in catalysis). They have shown success as catalysts in a variety of thermo-, redox-,

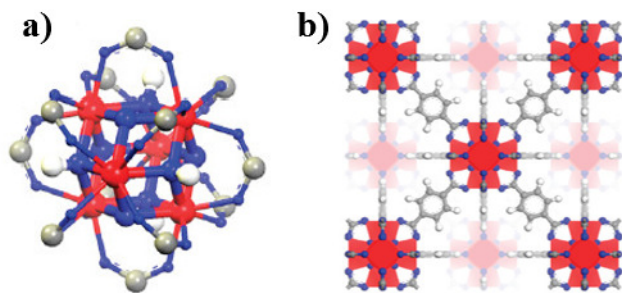


Figure 1.1: MOF UiO-66, which has $Zr_6O_4(OH)_4$ nodes and 1,4- benzenedicarboxylate (BDC) linkers. (a) $Zr_6O_4(OH)_4$ node. (b) Full crystal structure. Color key: Zr=red, O=blue, C=gray, and H=white. Adapted with permission from J. Am. Chem. Soc. 2008, 130, 42, 13850–13851. Copyright 2008 American Chemical Society

and photo-catalytic reactions, including hydrogenation, dehydrogenation, epoxidation, oligomerization, dehydration, esterification, condensation, and hydrolysis, as detailed in several recent reviews [16, 17, 18, 19]. Their modular design yields countless hypothetical structures, and their organic nature promotes tunability, which gives them significant potential as catalysts [20].

Catalytically active sites in MOFs are often metal entities. For example, the metal cations within the node can become catalytically active by removal of terminally coordinated solvent molecules [21] or by creation of “missing linker” defects [22]. Both strategies result in coordinatively unsaturated metal cations which can act as Lewis acids due to having vacant orbitals that accept electrons for bonding with reaction intermediates [23]. In addition, single metal cations [24], metal cation clusters [25], and metal cation complexes [26, 27] can be installed post-synthetically onto MOF nodes and linkers [28, 29] using solution-phase and vapor-phase methods such as transmetalation, metal doping, and atomic layer deposition (ALD) [30, 31]. In any case, the organometallic nature of MOFs provide spatial and electronic separation between metal entities, which facilitates synthesis and characterization and

promotes stability by preventing metal agglomeration [32]. A key advantage of MOF-based catalysts is that, like enzymes, the metal entity and ligand environment can be precisely tuned to achieve high activity and selectivity for desired chemistry. In combination with experimental characterization, computational modeling in MOFs is an invaluable tool and has been shown in previous works [33] to provide valuable insights that have led to improved MOF catalysts.

1.3 MOF NU-1000

The MOF NU-1000 has been used for a wide range of applications including heterogeneous catalysis [34, 24, 35]. It is comprised of $Zr_6(\mu_3\text{-OH})_4(\mu_3\text{-O})_4(\text{OH})_4(\text{OH}_2)_4$ nodes connected by tetratopic 1,3,6,8-tetrakis (p-benzoate) pyrene linkers (figure 1.2) [36, 37]. It has uniform hexagonal channels with diameter 31Å and triangular channels with diameter 10Å that penetrate layers separated by smaller pores (of diameter 8Å) along the c direction. The comparatively large (31 Å) mesoporous channels extending throughout the structure enable rapid diffusion of guest species throughout the framework [31]. It has high thermal (up to 500° C) and chemical stability (stable in aqueous and acid solutions as well as organic solvents) that can be attributed to strong bonding between the zirconium nodes and the carboxylates groups of the linkers [38]. The uncoordinated Zr_6 nodes act as Lewis acids and provide isolated reactive sites for chemical reactions. In addition, single metal cations [24], metal cation clusters [25], and metal cation complexes [26, 27] have been installed by post-synthetic treatment in NU-1000 [28, 29, 39, 40]. Hypothetically, the metal-organic nature and crystalline structure of NU-1000 can maintain spatial and electronic isolation of the metal cations and thus prevent metal agglomeration and sintering. These NU-1000 supported catalysts have previously been shown to be active for the methane

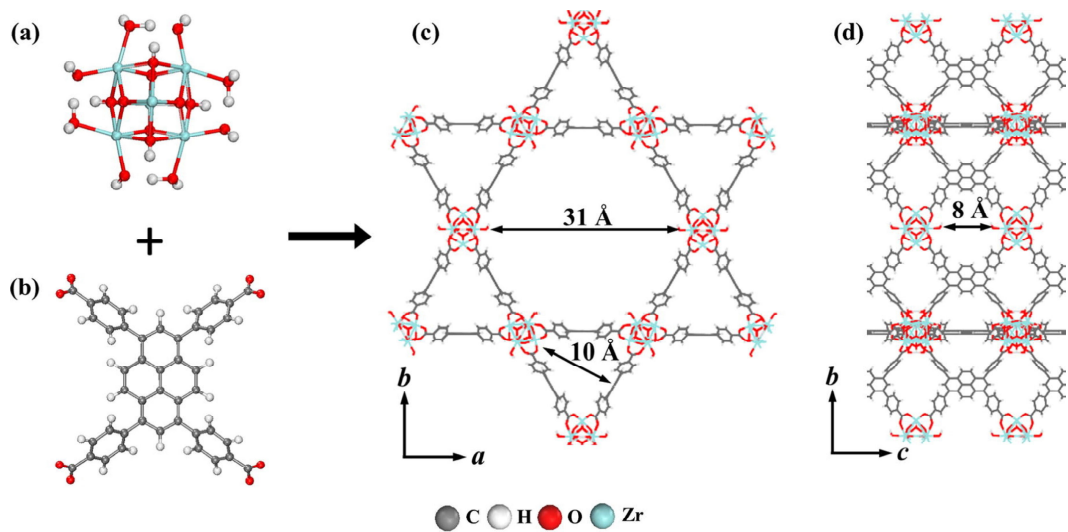


Figure 1.2: Schematic representation of crystal structure of NU-1000. The metal node is the (a) $\text{Zr}_6(\mu_3\text{-OH})_4(\mu_3\text{-O})_4(\text{OH})_4(\text{OH}_2)_4$ connected by (b) organic tetratopic 1,3,6,8-tetrakis (p-benzoate) pyrene linkers, (c) the hexagonal and triangular channels along the c direction, and (d) the small pore bridging the ab layers along the c direction. Color key: Zr=cyan, O=red, C= gray, H=white. Adapted with permission from J. Catal, 2017, 354, 278-286. Copyright 2017, Elsevier B.V.

to methanol, ethene to ethane, ethene to butene, propyne to propylene, and propane to propene reactions [41, 42, 43, 34, 24, 35].

In this work we investigate several applications of NU-1000 as a catalyst. Specifically, we investigate metalating it to act as a catalyst itself, as well as using it to encapsulate/stabilize other metal organic materials that act themselves as catalysts. The goal of this work is to develop computational models for metal cation-based catalysts supported in MOFs validated by experimental data to explain the trends in

activity of catalysts and their structure for GTL reactions. Through this work we have built models of the active sites to compute energetics of the reaction, microkinetic modeling for the rates of reactions and analyzing the impact of modeling choices. NU-1000 has been considered exclusively as a catalyst support in this work for single metal ions and metal-oxo clusters, however the inferences derived in this work can be applicable to most MOFs particularly Zr-based MOFs like UiO-66/67/68.

1.4 Dissertation Outline

Chapter 2 provides details of the computational model and the methods used in this work. Further details of experimental data and specific modeling choices are given in the methods sections of the individual chapters 3, 4 and 5.

Chapter 3 develops kinetic reaction model for single metal cation catalyst supported in NU-1000 for ethene hydrogenation as a test reaction. This model is first validated by experimental results and based on it an alternate mechanism in-line with experimental data for high spin metals is proposed.

Chapter 4 builds models of the active site for metal-oxo cluster based catalysts supported in NU-1000 along with the computational insights from the modeling.

Chapter 5 explores the impact of modeling choices for ethene dimerization as a test reaction.

Chapter 6 summarizes the conclusions from chapters 3-5 with recommendations for future research.

Chapter 2

Methods

2.1 Overview of Computational Modeling Techniques in MOFs

In the category of nanoporous materials, MOFs are comparatively a new synthetic material that have been primarily studied for their adsorption applications. Their catalytic applications have come to the forefront only recently. Hence computational modeling methods for studying MOFs are not as well-established as for more traditional supported metal catalysts. This overview briefly summarizes and explains the rationale for choosing computational catalysis methods in determining the active site and kinetics in MOFs used in this work.

2.1.1 Modeling the active site

A primary step in molecular simulations of any catalytic reaction is to compute the energetics (reaction energies and activation barriers) for steps that are hypothesized to play a significant role in the mechanism. This requires developing a model

of the active site and using quantum mechanics (QM) to compute the energies of potentially relevant reaction intermediates [44]. Active site models usually include a significant portion of the catalyst atoms to be reasonably chemically accurate while still maintaining computational tractability. Sometimes, models of the MOF catalysts employ the entire MOF unit cell; usually models of the active sites are truncated clusters [45] that capture the chemistry at the active site but cannot capture framework effects [24, 46]. This is to decrease the significant computational expense in modeling hundreds of atoms in a MOF unit cell. We have used both small cluster and large periodic models to model the active site consistent with prior works [24, 46].

2.1.2 Calculating Reaction Energetics

In this work we have used the QM method density functional theory (DFT) [47] for computing the energies of reaction intermediates. QM calculations of MOF catalysts are additionally challenging since catalytically active sites in MOFs involve transition metal cations, which have partially filled d orbitals with nearly degenerate energies. This presents multiple challenges. For one, calculating the energetics of such systems requires multiconfigurational methods [48, 49] which, while currently applicable for cluster models comprising a small number of atoms (<15) [50, 24], are presently too computationally demanding for use in larger systems, including periodic models. DFT is a computationally tractable option for simulating these systems with reasonable accuracy.

Another issue with modeling catalysis particularly on 3d transition metals is that they are prone to changing their spin states over the course of a reaction [49]. When this happens, a diabatic electronic potential energy surface (PES) results; the transition from one spin state (PES) to the other involves an activation energy which

couples with the activation energy associated with the chemical reaction [51]. In practice, this phenomenon is often ignored, and the activation barriers of such “spin forbidden” reactions are estimated by simply taking the difference between the energy of the transition state and the energy of the reactants, each in their lowest energy spin state (which are different from each other). This is the strategy we have also used in this work.

2.1.3 Accounting for Molecular Configurational Effects

In this work we have accounted for the probability of reactants adsorption and the specific configurational effects by molecular dynamics (MD) and *ab-initio* molecular dynamics (AIMD) for calculating the adsorption rate constants. In general, calculating the energy of a reaction intermediate requires generating a guess of a starting structure. Normally, this guess is a hypothesis based on the geometry that would minimize the intermediates’ electronic energy when binding to the active site, and the intermediate geometry is found by relaxing the guess geometry into the lowest energy geometry using QM. However, this approach neglects the multiple configurations in which molecules can approach and adsorb to the active sites in MOF catalysts. Host–guest interactions between fluid-phase molecules and the MOF acts to stabilize multiple molecular configurations near the active site, which can influence how the molecules coordinate with the active site. As MOFs have long been studied as sorbents, there are multiple force fields (FFs) for simulating host–guest interactions [52] that could be used to explore this configurational space in order to more accurately predict molecular configurations. The challenge in most MOF force-fields is that they do not accurately capture the interaction of the metal binding site with the guest molecule. To remedy that we have combined MD and AIMD simulations

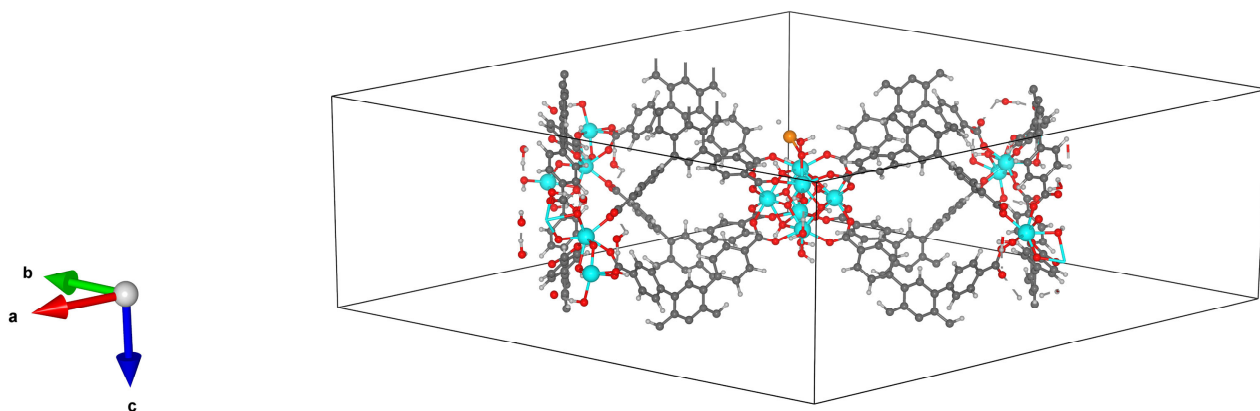


Figure 2.1: Simulation Box that is also the Unit cell of NU-1000 with lattice constants $a = b = 39.897 \text{ \AA}$, $c = 16.635 \text{ \AA}$, $\alpha = \beta = 90^\circ$, $\gamma = 60^\circ$. Ni =orange Zr=cyan O=red C=gray H=white.

to sample the configurational space near the metal site.

2.2 Catalyst Models

There are two types of models used in this work. First is a periodic model that comprises of the unit cell of NU-1000 (figure 2.1) with lattice constants $a = b = 39.897 \text{ \AA}$, $c = 16.635 \text{ \AA}$, $\alpha = \beta = 90^\circ$, $\gamma = 60^\circ$. This is used in the periodic DFT simulations, molecular dynamics (MD) simulation, *ab-initio* molecular dynamics (AIMD)

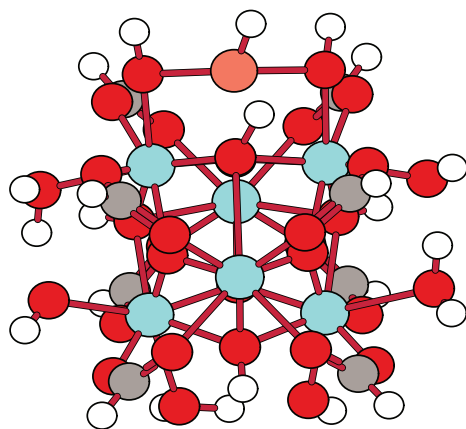


Figure 2.2: Truncated Zr-node of NU-1000 with installed Metal cations (Fe/ Mn/ Fe/ Co/ Ni/ Cu/ Zn) =orange Zr=cyan O=red C=gray H=white

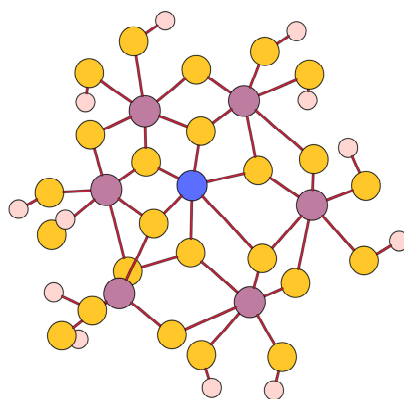


Figure 2.3: A Model of sulfided Cobalt Molybdenum Oxide catalysts for HER reaction with Co=blue Mo=purple S=yellow

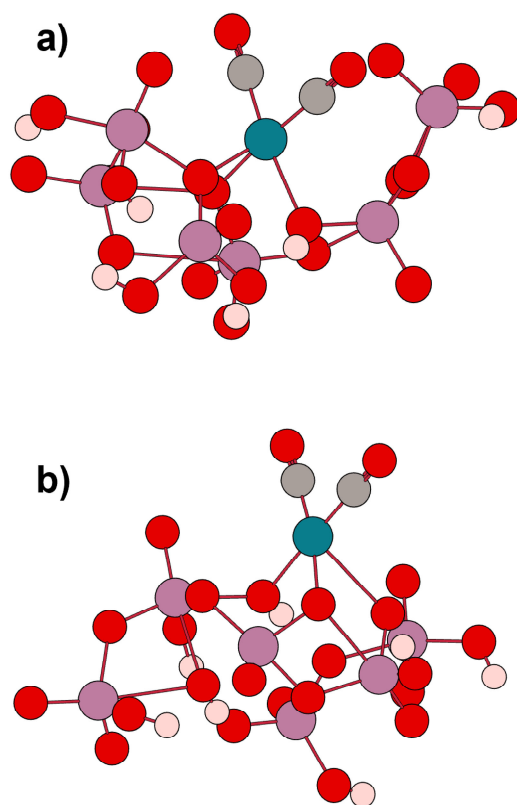


Figure 2.4: Two cluster models a) charged and b) uncharged of Rh Molybdenum Oxide catalyst for CO oxidation with Rh=dark teal Mo=purple O=red

simulations and grand-canonical monte carlo (GCMC) simulations (with twice the c-axis for the minimum image convention). This model has Zr nodes as well as pyrene linkers of NU-1000 and most accurately represents the structure of NU-1000. Second are the smaller cluster models for decreasing the computational expense from using the larger periodic model. They comprise of a) truncated clusters from the periodic model (figure 2.2) that have a single Zr node with pyrene linkers approximated as carboxylate groups and b) general cluster models (figures 2.4, 2.3).

2.3 Simulation Methods

All computations were done on the Palmetto super-computing cluster at Clemson University. The general details of each calculation are given below with specific details in individual chapters.

2.3.1 DFT Calculations in Gaussian-09

Gaussian-09 [53] was used to compute electronic energies and free energies of cluster models in order to learn about catalytic energetics and mechanisms. Structures, energies, and vibrational frequencies in Gaussian-09 are calculated with electron exchange and correlation (XC) modeled using the M06-L density functional [54, 55] and the PBE density functional [56]. Wavefunctions are expanded using the Def2-SVP basis set for H, C, S and O atoms; the Def2-TZVPP basis set for the metal atoms Mn, Fe, Co, Ni, Cu and Zn; and the Def2-TZVPP basis set with the associated effective core potential for Zr, Mo and Rh atoms [24, 46, 57, 58]. The Berny algorithm [59] is used for both geometry optimizations and transition state searches along with the default convergence criteria. Vibrational frequencies are calculated for all structures to verify their natures as local minima or transition states on the

potential energy surface. A sample calculation input file is given in Appendix A.

2.3.2 DFT Calculations in CP2K

CP2K [60] was used to compute electronic energies and free energies of the periodic models in order to learn about catalytic energetics and mechanisms. The exchange–correlation energy was calculated using PBE functional [56] with the D3 damped dispersion corrections of Grimme et al [61]. The DZVP-MOLOPT basis set, a plane wave cutoff energy of 360 Ry, and pseudopotentials for core electrons (as formulated by Geodecker et al [62]) were used. Further details of the parameters for the DFT calculations are given in the paper by Ye et al [25]. A sample calculation input file is given in Appendix A.

2.3.3 Partition Function calculations with Tamkin

All partition functions used in microkinetic modeling are calculated with the TAMkin package [63]. Vibrational partition functions are constructed using frequencies calculated in DFT. Specifically, the partition functions are constructed using frequencies associated with the atoms in the adsorbed species and the active site only. For structures calculated with M06-L and PBE in Gaussian-09, all frequencies with values below 50 cm^{-1} are replaced with 50 cm^{-1} to correct for the overestimation of the entropy contribution due to the known breakdown of the harmonic oscillator approximation for low-frequency vibrational modes [64]. Further, for M06-L, all frequencies with values above 50 cm^{-1} are scaled by 0.976, as in prior work [46], due to the tendency of the DFT method to overestimate vibrational frequencies [65, 66]. For structures calculated with PBE in Gaussian-09 the vibrational and the zero-point energies were corrected by 1.0295 and 1.0160 [67] respectively. For structures calculated

with PBE in CP2K, all frequencies with values below 50 cm^{-1} are replaced with 10 cm^{-1} to reproduce previous calculations [25] with no scaling for vibrational frequencies and the zero-point energies due to non-availability of these factors in literature for these parameters.

2.3.4 Parameters for GCMC and MD simulations

The TraPPE united-atom force field was used to describe ethene and n-butene [68]. Lennard-Jones parameters from the Dreiding force field [69] were used for carbon, oxygen, and hydrogen atoms in the NU-1000 framework, whereas UFF [70] was used for the Zr and Ni atoms. The potential was truncated at the cutoff distance of 12\AA . Full periodic boundary conditions were in effect in three dimensions. Framework atoms were fixed (immobile) at their crystallographic coordinates and only the adsorbates were mobile.

2.3.5 GCMC Simulations in RASPA

GCMC simulations were done to get the number of ethene molecules at specific temperature pressures and ethene concentration at the unit cell of NU-1000. This is to correct the results from single molecule ethene MD simulations Adsorption isotherms were obtained in the grand canonical ensemble with RASPA [71] to establish the relationship between temperature, pressure and loading of ethene in NU-1000. Simulations of hydrocarbons in MOFs using the aforementioned parameters have been shown to produce adsorption isotherms that agree well with experimental results [72]. The MC simulations proceeded for 50,000 cycles of equilibrium followed by 100,000 of production, where a cycle is max (20,N)-move attempts, with N being the number of molecules [73, 74]. The MC moves used were translation, rotation, insertion and

deletion with configurational bias (CBMC). We monitored the energy as well as the loading to verify that this number of cycles was appropriate to reach equilibrium. To satisfy the minimum image convention the unit cell of NU-1000 was multiplied by 2 on the c-axis. A sample calculation input file is given in Appendix A.

2.3.6 MD Simulations in LAMMPS

Molecular dynamics (MD) simulations were performed in LAMMPS [75]. The equations of motion were integrated using the velocity Verlet scheme [76] with a 1.0 fs time step in the NVT ensemble using a Nose-Hoover thermostat [77] with the temperature kept fixed at 300K. The average values of temperature and energy were monitored through the whole run of the simulation to make sure there were no major fluctuations.

2.3.7 AIMD Simulations in CP2K

AIMD [78, 79] is a method where the potential energy surface (PES) is calculated every step from first principles electronic structure methods to generate finite temperature molecular dynamics (MD) trajectories. This limits sampling larger trajectories due to high computational cost of DFT calculations but yields energies and trajectories with quantum accuracy. AIMD simulations were done in CP2K [60]. For the electronic structures method we used DFT with the parameters in section 2.3.2 and Ye et al [25]. For the MD part of the simulations the NVT ensemble with a Nose-Hoover thermostat [77] was used with a time step of 1 femtosecond. All simulations were run for 300-1000 femtoseconds at a temperature of 300K, with coordinates extracted at every 1 femtosecond. A sample calculation input file is given in Appendix A.

Chapter 3

Microkinetic Modeling of Ethene Hydrogenation on Single-site Cation Catalysts Supported in NU-1000

3.1 Introduction

In this chapter, we investigate metal cation catalysts supported on NU-1000 for upgrading light hydrocarbons found in natural gas (published in the paper [44]). Converting light hydrocarbons to liquid alkanes and short-chain alkenes requires an understanding of C–C and C–H bond chemistry. As a step toward understanding this chemistry in MOF catalysts, we investigate C–H bond chemistry in this chapter. Specifically, we interrogate the mechanism of ethene hydrogenation to ethane, $\text{C}_2\text{H}_4(\text{g}) + \text{H}_2(\text{g}) \longrightarrow \text{C}_2\text{H}_6(\text{g})$. Given their wide use in promoting reactions involved in upgrading light hydrocarbons, our study focuses on isolated single-site metal cation-

based catalysts, specifically Mn^{2+} , Fe^{2+} , Co^{2+} , Ni^{2+} , Cu^{2+} , and Zn^{2+} supported on NU-1000 designated as M@NU-1000 . Designing catalysts for any reaction requires understanding the reaction mechanism, as this enables the catalyst to be optimized to promote the desired chemistry. Despite the growing body of literature on conversions of light hydrocarbons on M@NU-1000 catalysts, relatively little is known about their reaction mechanisms. In fact, the only metal cations for which collaborative experiments and simulations have been performed in order to understand the reaction mechanisms are Ni@NU-1000 (ethene hydrogenation and ethene dimerization) and Co@NU-1000 (ethene dimerization) [24, 35]. In the case of ethene hydrogenation for Ni@NU-1000 catalysts, Li et al. used a combination of in situ X-ray absorption spectroscopy (XAS) characterization and density functional theory (DFT) calculations to learn the mechanism on Ni@NU-1000 [35]. They concluded that the mechanism follows a cycle proposed by Schroeder and Wrighton [80] for photocatalytic olefin hydrogenation on homogeneous metal cation complexes. This mechanism, which from here on out, we refer to as the SW mechanism, is illustrated in figure 3.1. Briefly, the active site is a metal hydride. Ethene C_2H_4 (g) adsorbs to the active site (1 in figure 3.1 and rxn (3)) and then reacts with the metal hydride (2 in figure 3.1 and rxn (7)), forming an ethyl moiety, C_2H_5 . Hydrogen H_2 (g) then adsorbs to the active site (3 in figure 3.1 and rxn (2)) and reacts with C_2H_5 to form ethane C_2H_6 in a concerted H_2 dissociation/C–H bond formation (4 in figure 3.1 and rxn (9)). The C_2H_6 then desorbs (5 in figure 3.1 and rxn (4)) to regenerate the metal hydride.

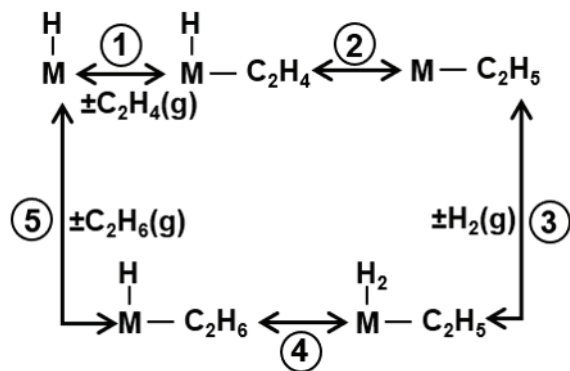


Figure 3.1: The SW mechanism. M = metal cation.

3.2 Methods

3.2.1 Experimental Methods and Results

Our collaborators synthesized NU-1000 and modified it by atomic layer deposition (ALD) to install 6 metal cations (Mn^{2+} , Fe^{2+} , Co^{2+} , Ni^{2+} , Cu^{2+} and Zn^{2+}). Catalytic experiments were conducted to monitor the rate of ethane formation from hydrogen and ethene over a temperature range of 50-200°C at a pressure of 1 atm (figure 3.4a). Details of these methods are given in this paper [44]. A reasonable question is whether the installed metals remain cationic during the hydrogenation experiments (i.e., resist agglomeration into metal nanoparticles). Prior publications based on X-ray absorption near edge structure (XANES) and extended X-ray absorption fine structure (EXAFS) on Ni@NU-1000 indicate that the cationic Ni^{2+} state and the corresponding Ni-O bonds are largely preserved after exposure to H_2 at 200°C, with the most major change in the Ni oxo structure due to formation of a small amount of Ni hydride [35]. Further, XAS and EXAFS of Cu@NU-1000 reveals that the installed Cu remains cationic below 200°C in a H_2 environment [81]. As the free energies of reduction of Mn, Fe, Co, and Zn cations to neutral metals are higher (more

positive) than for Ni and Cu, we assume that these metals also retain their cationic states under the hydrogenation conditions employed in our experiments and do not agglomerate into metallic nanoparticles. NU-1000 synthesis and post-modification with metal cations were carried out using previously reported methods [82, 31]. Installation of metal cation catalysts occurs at the nodes (circled in figure 3.2a) and is accomplished using either vapor phase or solution techniques [39, 40]. The vapor phase atomic layer deposition (ALD) in MOFs (AIM) technique is used to create the catalyst samples. Prior to AIM, the Zr_6 nodes present nearly four equivalent faces. Each face has surface chemistry amenable to reaction with up to two metal ALD precursors. According to previously reported processes, AIM results in porous frameworks with 4 to 8 installed metal ions per Zr_6 node [40]; therefore, each face comprises 1 or 2 metal cations. The installed metal ions replace two protons on a set of hydroxy/water ligands on the node but do not replace the Zr ions.

3.2.2 Computational Methods

3.2.2.1 Catalyst Model

Calculations in this chapter utilize models comprising a truncated NU-1000 node with an installed metal cation (figure 3.2b), similar to prior work [39, 40, 46]. While there is the question as to whether the NU-1000 node comprises of one or more metal cations, prior literature based on DFT analysis of the reaction mechanism of ethylene dimerization at the Ni oxo sites on Ni@NU-1000 catalysts indicates that the Ni cation spin state influences the results more than the nuclearity of the Ni oxo clusters, with models including one Ni cation giving nearly identical results as models comprising four Ni cations, as long as the Ni cations are modeled in the same spin state [25]. Our models thus comprise one metal cation per node. The installed metal

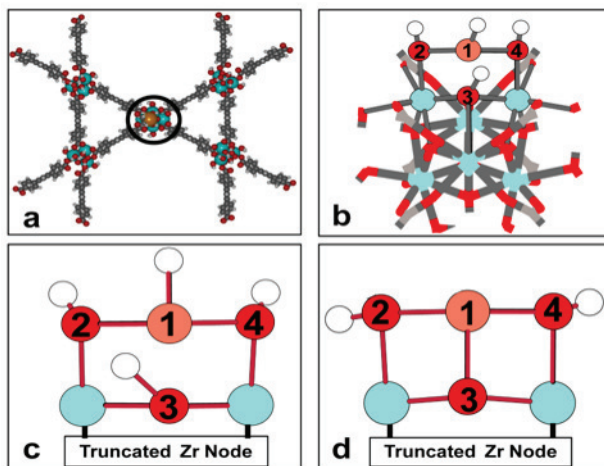


Figure 3.2: a) The NU-1000 crystal structure with the node circled. b) The catalyst model employed in this chapter. c) Metal hydride active site. d) Bare metal cation active site. Color key: carbon = gray, oxygen = red, hydrogen = white, zirconium = teal, metal cation = orange. In b), c) and d), atoms labeled 1, 2, 3, and 4 represent the different sites where hydrogen species are allowed to bind in the density functional theory calculations

cations have formal charges of 2+ (i.e., the installed metals are dicationic). Prior to metalation, the truncated node model has a net formal charge of 0. The metal cations take the place of two protons on the node; hence, installation of the metal cations does not change the net formal charge of the model. Catalytic species are allowed to bind to the metal cation along with its proximal oxo and hydroxy ligands. The atoms where catalytic species are allowed to bind make up the active sites in our models. In all, we evaluate five different active sites (illustrated in figure S1 in the ESI of reference [44]).

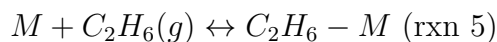
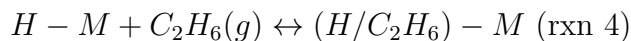
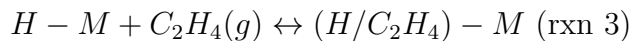
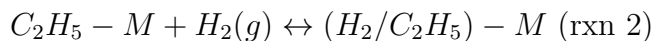
The distinction among different active sites is the arrangement of hydrogen species on the metal cation and proximal oxo and hydroxy ligands. Our findings suggest that Mn@NU-1000, Fe@NU-1000, Co@NU-1000, Ni@NU-1000, Cu@NU-1000, and Zn@NU-1000 use the active site compositions illustrated in figures 3.2c and 3.2d for ethene hydrogenation. Specifically, figure 3.2c is the metal hydride active site

utilized in the SW mechanism by Ni@NU-1000, Cu@NU-1000, and Zn@NU-1000, and figure 3.2d shows the bare metal cation active site as being utilized by Mn@NU-1000, Fe@NU-1000, and Co@NU-1000.

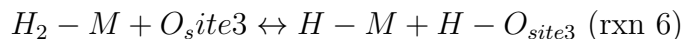
3.2.2.2 Reaction Steps

In all, we evaluate 22 reaction steps for each M@NU-1000 catalyst using microkinetic modeling. Nine of the reaction steps that we consider are illustrated in figure 3.3 and listed below. The rest are described in the ESI in figures S2 and S3 and table S2 of reference [44]. Reaction steps that utilize the ‘/’ notation (e.g., rxns 2, 3, 4 and 7 listed below) denote co-adsorption, as in prior work [46]. For example, (H₂/C₂H₅)-M in rxns 2 and 9 indicates that H₂ and C₂H₅ are co-adsorbed to the metal cation site. The steps shown in figure 3.3 and listed below are the ones identified in microkinetic modeling as belonging to a reaction mechanism followed by the catalysts studied in this chapter. Reaction steps within the SW mechanism are highlighted in figure 3.3.

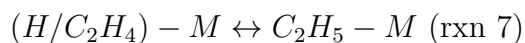
Adsorption/Desorption:



H₂ Dissociation:



C-H Bond Formation:



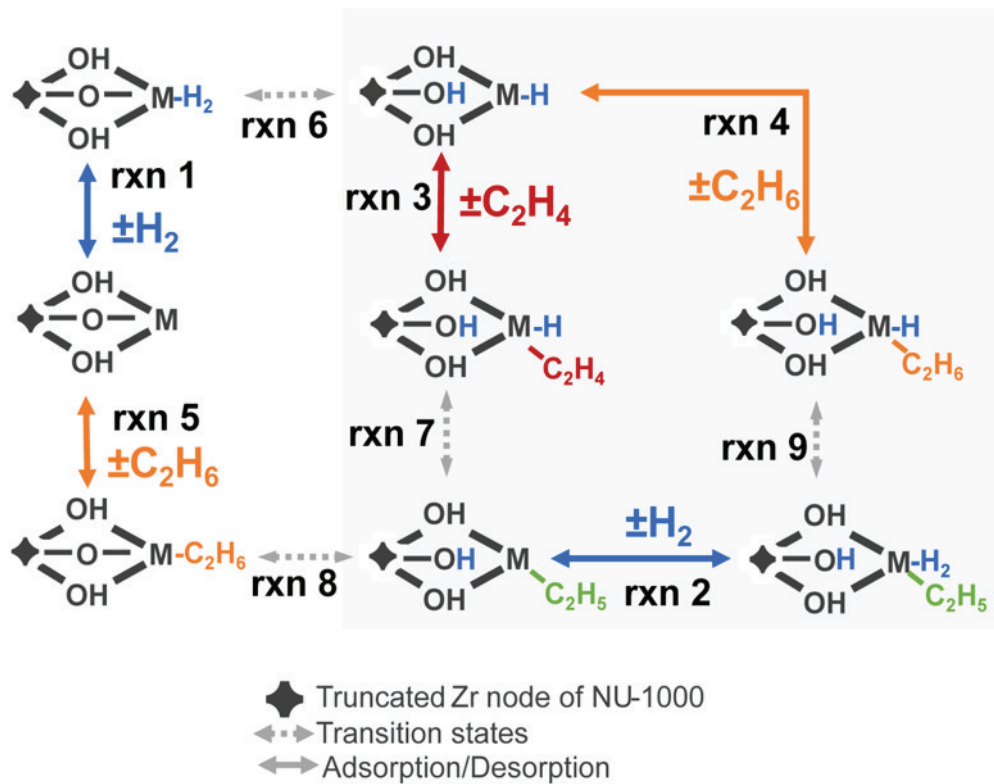
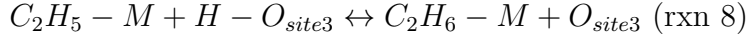
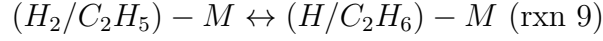


Figure 3.3: Reaction steps followed by the metal cation catalysts studied in this chapter. Rxn numbers correspond to those in the text. The SW mechanism is highlighted.



Concerted H₂ Dissociation/C-H Formation:



3.2.2.3 Microkinetic Modeling

Microkinetic modeling is carried out using the MKMCXX program [83, 84, 85]. Similar to experiments, microkinetic models are run over temperature ranges of 50-200°C. The total pressure is set to atmospheric and comprises 0.75% ethene and 2.25% hydrogen in a balance of inert gas. All pressures are held constant over the course of simulation. Since ethane is not introduced into the system, this represents the case where the conversion of ethene equals zero. Each simulation is run for 10⁸ s and considered to be converged when the changes in the fractional concentrations of all of the reaction intermediates between successive iterations are less than 10⁻¹². Adsorption (k_{ads}) and desorption (k_{des}) rate constants are calculated as [85] A sample calculation input file is given in Appendix A.

$$k_{ads} = \frac{yPA}{\sqrt{2\pi mk_bT}} \quad \dots \text{eq. 1}$$

$$k_{des} = \frac{k_bT^3}{h} \frac{A(2\pi mk_bT^3)}{\sigma \Theta_{rot}} e^{\frac{-E_{des}}{k_bT}} \quad \dots \text{eq. 2}$$

$$k_{surf} = \frac{k_bT}{h} \frac{Q^{TS}}{Q} e^{\frac{-E_a}{k_bT}} \quad \dots \text{eq. 3}$$

where E_a is the activation barrier calculated in DFT, and Q^{TS} and Q are the vibrational partition functions for the transition state and reactant, respectively. In cases where $E_a < 0$, it is set to 0 in eq. 3. Partition functions are calculated with TAMkin (2.3.3).

3.2.2.4 DFT Calculations

All DFT calculations are done with the software Gaussian-09 with the M06-L density functional (section 2.3.1) [54, 55]. The total charge on the truncated node models with installed cations is set to 0 in all DFT calculations. During geometry optimizations and transition state searches involving NU-1000, the carbon atoms on the benzoate groups on the catalyst model are kept fixed to simulate the structural rigidity of the NU-1000 framework [46, 57]. Multiple possible spin-states for Mn@NU-1000, Fe@NU-1000, Co@NU-1000, and Ni@NU-1000 are considered. Cu²⁺ and Zn²⁺ only have one possible spin state each, i.e., doublet and singlet, respectively; hence Cu@NU-1000 and Zn@NU-1000 are only modeled in these spin states. Specifically, Mn@NU-1000 is modeled as a quartet and a sextet, Fe@NU-1000 as a triplet and a quintet, Co@NU-1000 as a doublet and a quartet, and Ni@NU-1000 as a singlet and a triplet. We did not include the doublet and singlet structures for Mn@NU-1000 and Fe@NU-1000, since these spin states are not energetically favorable. Unless indicated otherwise, microkinetic modeling results use the spin state that gives the lowest energy for each structure, as in prior work [46]. For these intermediates, the total spin is within 10% of the expected values, indicating minimal spin contamination. The calculated energies of all catalytic species considered in this chapter are provided in tables S3 and S4 in the ESI of reference [44].

3.3 Results

The rates of ethane formation observed in high throughput reactor studies and calculated in microkinetic modeling are plotted as functions of temperature in figure 3.4. The experimental rates (figure 3.4a) include contributions from the metal cations as well as from NU-1000 itself; catalytic studies performed on a non-metallated NU-

1000 sample indicate NU-1000 contributes $\sim 10^{-10}$ moles of ethane produced per second to the observed rates, compared to $\sim 10^{-7}$ moles of ethane produced per second on Ni@NU-1000 and 10^{-9} moles of ethane produced per second on Cu@NU-1000. Simulated rates using the SW mechanism (5 total rxn steps; see figures 3.1 and 3.3) are plotted in figure 3.4b.

Comparing figures 3.4a and 3.4b, Ni@NU-1000 gives the highest rate of all the metals, while Zn@NU-1000 gives the lowest. The rank order for rate observed experimentally is Ni@NU-1000 > Co@NU-1000 > Cu@NU-1000 > Mn@NU-1000 > Fe@NU-1000 > Zn@NU-1000, whereas the trend simulated using the SW mechanism is Ni@NU-1000 > Cu@NU-1000 \sim Mn@NU-1000 \sim Fe@NU-1000 > Co@NU-1000 > Zn@NU-1000. Notably, Co@NU-1000 is observed experimentally to exhibit a high rate; however, in figure 3.4b, Co@NU-1000 exhibits a relatively low rate. This disagreement between experiment and simulations prompted us to explore the expanded reaction network involving proximal oxohydroxy groups discussed above (22 total rxn steps; see figure S2 in the ESI of reference [44]). In doing this, the mechanism for each catalyst is revealed in microkinetic modeling, which reduces the number of assumptions in the simulations. Simulated rates employing the expanded reaction network are shown in figure 3.4c. Using this expanded reaction network, the rank order for rate is Ni@NU-1000 > Mn@NU-1000 > Co@NU-1000 > Fe@NU-1000 > Cu@NU-1000 > Zn@NU-1000. Notably, using the expanded reaction network, Co@NU-1000 exhibits a high rate, as observed experimentally. The experimental trend in catalytic activity is also more closely reproduced, with the exception of Mn@NU-1000.

Analysis of the microkinetic modeling results indicates that Ni@NU-1000, Cu@NU-1000, and Zn@NU-1000 follow the SW mechanism (Cu@NU-1000 actually follows the SW mechanism up to 150°C, above which it follows a different mechanism; see Section S1 in the ESI of reference [44]), while Mn@NU-1000, Fe@NU-1000, and

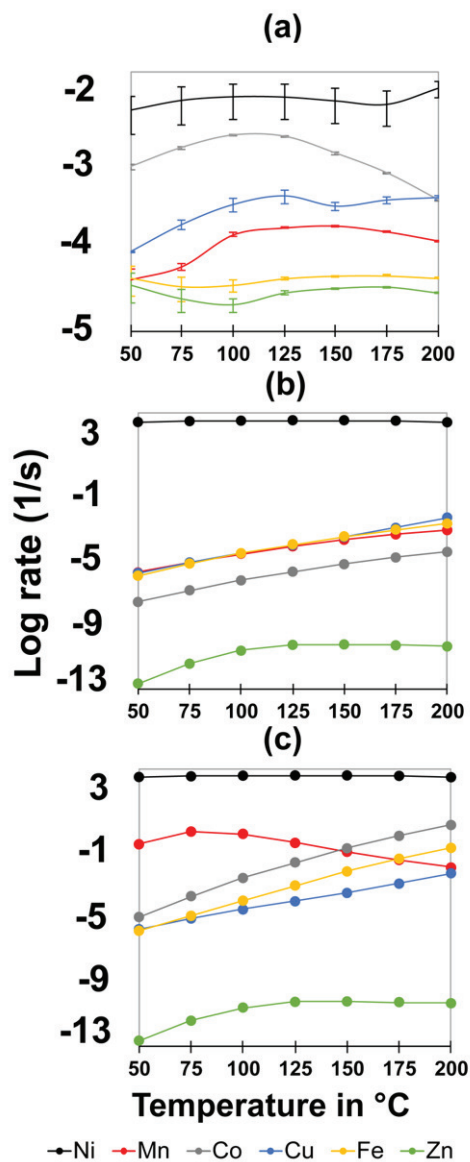


Figure 3.4: Log rates in units of moles of ethene converted per metal cation site per second. (a) Experimentally measured. (b) Rates simulated in microkinetic modeling including only the 5 steps that comprise the SW mechanism. (c) Rates simulated using all 22 steps considered in this chapter.

Catalyst	Spin state	Preferred mechanism
Mn@NU-1000	Quartet	SW
	Sextet	Alternate
Fe@NU-1000	Triplet	SW
	Quintet	Alternate
Co@NU-1000	Doublet	SW
	Quartet	Alternate
Ni@NU-1000	Singlet	SW
	Triplet	SW
Cu@NU-1000	Doublet	SW
Zn@NU-1000	Singlet	SW

Table 3.1: Mechanism and active site preference for the different spin states considered in this chapter

Co@NU-1000 follow an alternate mechanism, illustrated in figure 3.3. This mechanism starts from a bare metal cation active site (figure 3.2d). H_2 adsorbs to this site (rxn 1) and dissociates via the use of a proximal oxo ligand (rxn 6), forming a metal hydride and converting the oxo to a hydroxy ligand. C_2H_4 adsorbs to (rxn 3) and reacts with the hydride (rxn 7), forming C_2H_5 . The C_2H_5 then reacts with the residual H from the proximal hydroxyl ligand to form C_2H_6 (rxn 8), which then desorbs (rxn 5) to regenerate the bare metal cation catalyst.

3.4 Discussion

3.4.1 Rationale for Mechanism Preference

In their lowest energy configurations, the preference of the different metal cations for the SW mechanism versus the alternate mechanism depends on the occupancy of the d shell of the metal cation. Specifically, Ni@NU-1000, Cu@NU-1000, and Zn@NU-1000, which have more electrons in their d shells, prefer the SW mechanism, whereas Mn@NU-1000, Fe@NU-1000, and Co@NU-1000, which have fewer electrons

	Mn@NU-1000	Fe@NU-1000	Co@NU-1000
SW (rxn (2))	$\Delta G = \mathbf{46}$	$\Delta G = \mathbf{4}$	$\Delta G = \mathbf{47}$
SW (rxn (2))	$\Delta G = -13$	$\Delta G = -9$	$\Delta G = -3$

Table 3.2: Calculated H₂ adsorption free energies on the metal hydride (rxn (2)) versus bare metal cation (rxn (1)) for Mn, Fe, and Co@NU-1000 catalysts in kJ/mol. Endergonic values are bolded

in their d shells, prefer the alternate mechanism. We show below that the preference for the SW or alternate mechanism depends on both the occupancy of the d shell and the spin state of the metal cation.

Of the M@NU-1000 catalysts that we studied, the lowest energy structures are for the most part high spin states (see table S3 in the ESI of reference [44]), meaning that the energy separation between neighboring d orbitals is small enough such that it facilitates placing two electrons in higher energy orbitals rather than placing each in same low-energy orbital, thereby allowing for a greater distribution of electron density across all of the d orbitals as compared to a low spin state. (The exceptions are Ni@NU-1000, which prefers the singlet state for all structures except the metal hydride, the transition state for rxn 7 on Co@NU-1000, which prefers the doublet spin state, and Cu@NU-1000 and Zn@NU-1000, which can only exist in one spin state, due to being d9 and d10 complexes, respectively).

To interrogate how this influences the mechanism, we re-ran our microkinetic model, this time instead of using the spin states that gave the lowest energy for each structure, we exclusively ran each spin state for each M@NU-1000 catalyst. The results (table 3.1 and figure S5 in the ESI of reference [44]) suggest that metals in low spin states prefer the SW mechanism, whereas metals in high spin states prefer the alternate mechanism. The switch of preference from the SW mechanism to the alternate mechanism happens at the quartet spin state. Catalysts that can

assume this spin state are Mn@NU-1000 and Co@NU-1000. While the Co@NU-1000 quartet prefers the alternate mechanism, the Mn@NU-1000 quartet prefers the SW mechanism, suggesting that the mechanism depends both on the spin state and the electron configuration of the metal cation. In this case, Mn@NU-1000, which has fewer d electrons, prefers the SW mechanism, while Co@NU-1000, which has more d electrons, prefers the alternate mechanism.

Calculated free energies along the SW and alternate mechanisms for Mn@NU-1000, Fe@NU-1000, and Co@NU-1000 are compared in figure 3.5. Analysis of these values suggests that the alternate mechanism exhibits faster rates because it provides a lower energy route for H₂ adsorption. Free energies for H₂ adsorption in the SW mechanism (rxn 2) are compared with those in the alternate mechanism (rxn 1) in table 3.2. Specifically, H₂ adsorption in the SW mechanism is endergonic on Mn@NU-1000, Fe@NU-1000, and Co@NU-1000, while H₂ adsorption in the alternate mechanism is exergonic on Mn@NU-1000, Fe@NU-1000, and Co@NU-1000. The low driving force for H₂ adsorption in the SW mechanism results in a lower hydrogenation rate. Prior literature on low spin Ni@NU-1000 versus high spin Co@NU-1000 catalysts for C₂H₄ dimerization indicates that the low spin Ni@NU-1000 catalyst is more active, since the greater availability (lower filling) of d orbitals allows more effective binding with catalytic species [24]. Specifically, using state-of-the-art multireference calculations, Bernales and co-workers showed that the low spin Ni@NU-1000 catalyst more effectively binds with C₂H₄ due to the availability of an unoccupied d orbital, which leads to a lower transition barrier for C-C bond formation. A similar argument could be made here for the case of H₂ adsorption in the alternate mechanism versus the SW mechanism. In the SW mechanism, H₂ adsorption (rxn 2) takes place on a metal cation with an adsorbed ethyl moiety. As the ethyl moiety is chemically bonded to the metal cation, it hybridizes with metal cation d electron density. This

	Mn@NU-1000	Co@NU-1000	Ni@NU-1000	Cu@NU-1000
Experiment	16	20	25	15
Microkinetic Modeling	58	110	4	56

Table 3.3: Apparent activation energies Mn, Co, Ni, and Cu@NU-1000 catalysts in kJ/mol

makes the metal cation less effective at binding with H₂. Indeed, Mulliken population analysis (see table S4 in the ESI of reference [44]) indicates that the bare metal cations in the Mn@NU-1000, Fe@NU-1000, and Co@NU-1000 catalysts have fewer d electrons, and hence a greater fraction of unoccupied d orbitals, than their analogs with adsorbed C₂H₅. Additionally, metal cation-H₂ bond distances are shorter on the bare metal cations than on the metal cations with adsorbed C₂H₅ (see table S4 in the ESI of reference [44]), further corroborating more effective hybridization on the bare metal cation sites. These results suggest that high spin metals prefer the alternate mechanism for hydrogenation because the bare metal cation site is more effective at binding H₂, resulting in more favorable H₂ adsorption free energies and hence faster rates.

3.4.2 Comparison of Apparent Activation Energies

To further test the validities of the proposed mechanisms, we compared measured apparent activation energies with simulated values from microkinetic modeling. Apparent activation energies were calculated for Mn@NU-1000, Co@NU-1000, Ni@NU-1000, and Cu@NU-1000 catalysts (table 3.3) between 50°C and either 75°C or 10°C (see the ESI of reference [44]), i.e., the regions in figures 3.4a and c where the logarithm of the rate either increases or remains constant with temperature. Details on how these values were calculated are provided in Section S5 of the ESI of reference

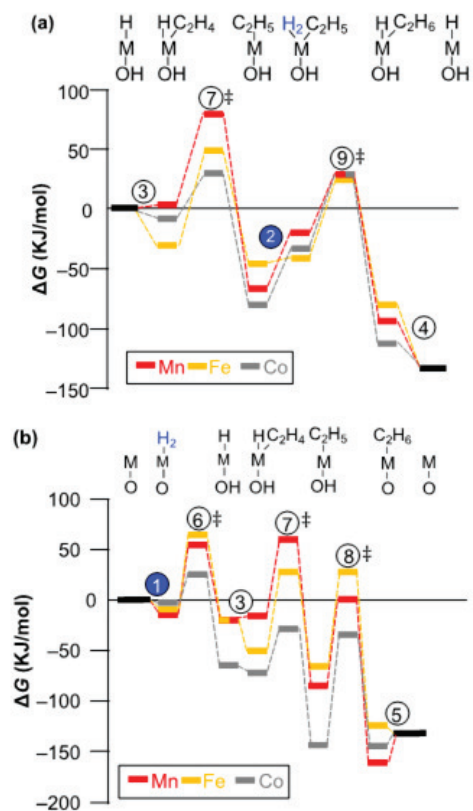


Figure 3.5: Log rates in units of moles of ethene converted per metal cation site per second. (a) Experimentally measured. (b) Rates simulated in microkinetic modeling including only the 5 steps that comprise the SW mechanism. (c) Rates simulated using all 22 steps considered in this chapter.

[44]. Insights from microkinetic modeling indicate that the catalysts are adsorption limited over the temperature range studied; this causes the rate to come to a maximum and then start decreasing with temperature. Such trends are seen in both the experimentally observed (figure 3.4a) and simulated (figure 3.4c) rates. Hence, the apparent activation energies could have contributions from the activation barrier of the rate controlling step as well as from the energy of desorption. From table 3.3, the trend in the experimentally measured apparent activation energies is Cu@NU-1000 \sim Mn@NU-1000 < Co@NU-1000 < Ni@NU-1000. The value for Ni@NU-1000 is in good agreement from previously reported studies [35]. The trend in the apparent activation energies derived from microkinetic modeling is Ni@NU-1000 < Cu@NU-1000 \sim Mn@NU-1000 < Co@NU-1000. Ni@NU-1000 is hence predicted by microkinetic modeling to have a relatively low apparent activation energy, while it is observed experimentally to have a high apparent activation energy; otherwise, the experimental and simulated trends are the same. Notably, Ni@NU-1000 is controlled largely by adsorption/desorption in the microkinetic modeling results. Comparing the apparent activation energy values between experiments and theory indicates a factor of at least 3.5 and to up to 6.6 between experiments and theory. The largest discrepancy is for Ni@NU-1000; we note that the highest activation barrier in the dominant reaction pathway for Ni@NU-1000 is 17 kJ/mol, which is in much better agreement with experiment. The discrepancy for the rest of the metals could be from multiple reasons. For example, even small differences in the energy of desorption between simulations and experiments could create significant inconsistencies in the temperature at which the catalysts become adsorption limited and thus how much of the apparent activation energy is due to desorption versus surface reaction (as in the case of Ni@NU-1000). Further, there could be steps with lower barriers than those proposed in this manuscript (e.g., a lower barrier alternative to rxn 8 on Co@NU-1000), which

have not yet been identified. In fact, some of the complexity in fully reconciling the mechanisms of M@NU-1000 catalysts is due to spin. Calculating energetics of catalytic species when there are multiple spin states possibly at play is computationally demanding (requiring multireference calculations) and theoretically challenging.

3.5 Conclusions

In this chapter, we compared microkinetic modeling with high throughput reactor studies performed by our collaborators to investigate the mechanism of ethene hydrogenation on metal cation catalysts supported on the MOF NU-1000. We found that metal cations with smaller numbers of unpaired electrons utilize a metal hydride active site and follow a mechanism previously proposed for catalytic hydrogenation on M@NU-1000 catalysts and homogeneous metal cation photocatalysts. In contrast, metal cations that have more unpaired electrons utilize a bare metal cation active site and employ proximal oxo ligands for binding of hydrogen species. Similar to prior work [24], the high spin metal cations seek mechanisms where the availability of unoccupied d orbitals is maximized, as this improves the hybridization with orbitals of gas phase species. In the case of catalytic hydrogenation, this leads to more effective binding of H₂.

Chapter 4

Structure Elucidation of Polyoxometalate Catalysts supported in NU-1000

4.1 Introduction

4.1.1 Background

In this chapter, we investigate polyoxometalate species stabilized within NU-1000 for the CO oxidation and hydrogen evolution reactions. Polyoxometalates (POMs) constitute a large class of polynuclear oxo-bridged early transition-metal compounds with a rich topology and versatile chemical and physical properties [86]. They are based on the assemblage of MO_n (M = addenda atoms e.g., W^{VI} , Mo^{VI} , V^V , Ti^{IV} , Nb^V , Ta^V) polyhedra, most commonly octahedra, interconnected via corner and edge sharing. Prominent subsets include Keggin $[\text{XM}_{12}\text{O}_{40}]^{n-}$ (10Å) [87], Dawson $[\text{X}_2\text{M}_{18}\text{O}_{62}]^{n-}$ (12Å) [88], and Anderson $[\text{XM}_6\text{O}_{24}]^{n-}$ (8.5Å) types [89, 90]

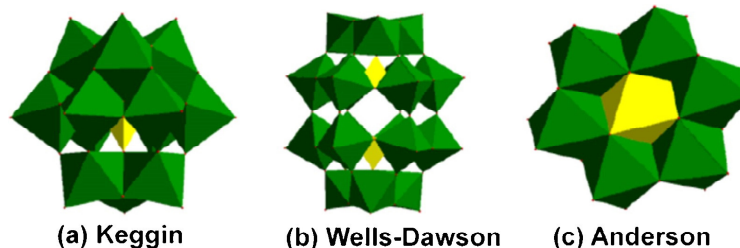


Figure 4.1: Classical POM structures in polyhedral representations. Adapted with permission from *Coord. Chem. Rev.*, 2015, 286, 17-29, Copyright 2014 Elsevier B.V.

POMs (figure 4.1).

The combination of adjustable structure, and manifold compositions has enabled polyoxometalates to be used as catalysts for a variety of oxidation reactions [91, 92]. These include water oxidation [93, 94], alkene epoxidation [95, 96, 97], aldehyde [97] and alcohol oxidation [19]. While they are exceptional oxidation catalysts, they tend to fall short for reduction reactions. Pure POMs typically offer limited active-site accessibility due to low surface area ($<10 \text{ m}^2/\text{g}$) [98], low melting points, and difficulties for separation in solution-phase reactions, thus limiting their catalytic utility. To overcome these limitations, porous supports such as mesoporous silica [99, 100], organic polymers [101, 102], covalent organic frameworks (COFs) [103], and MOFs [104, 105, 106] have been used to anchor POMs.

Since we are primarily interested in converting shale gas to liquids, we are using POMs stabilized in NU-1000 as scaffolds for developing catalysts for reductive chemistry. Taking inspiration from nature, that has enzyme co-factors containing

pairs or clusters of first-row transition metal ions coordinated in part by sulfur for reduction reaction [107, 108, 109, 110, 111, 112, 107, 108], developing metal-sulfide catalysts for reductive chemical transformation is an attractive option. For reduction reactions, synthetic access to sulfur-containing analogues of POMs the polysulfidometalates could open-up sites for reductive catalytic chemistry. In practice, there appears to be little or no extant literature on this topic.

4.1.2 Anderson POMs supported in NU-1000

Anderson POM catalysts supported in NU-1000 (i.e. polyoxometalate@NU-1000 and the sulfur-containing polysulfidometalate@NU-1000) were synthesized by our collaborators to demonstrate proof of concept of their catalytic activity for oxidation and reduction reactions [113, 114]. Anderson polyoxoanions are composed of six edge-sharing MoO_6 or WO_6 octahedra surrounding a central, edge-sharing heteroatom of octahedral geometry (XO_6) defining a planar arrangement having approximate D_{3d} symmetry. The general formula can be written as $[\text{H}_y(\text{XO}_6)_6\text{M}_6\text{O}_{18}]^{n-}$, where $y=0-6$, $n=2-8$, $M=$ addenda atoms (Mo^{VI} or W^{VI}), and $X=$ central heteroatom. The heteroatom can be any of several transition metals (Cr, Mn, Fe, Co, Ni, Cu, Zn, Pt, etc.) as well as certain main-group atoms (Te, I, Sb, etc.; see figure 4.2) [115].

Specifically, four catalysts $[\text{RhMo}_6\text{O}_{24}\text{H}_6]^{n-}@NU-1000$, $[\text{Mo}_7\text{O}_{24}\text{H}_6]^{m-}@NU-1000$, $[\text{CoMo}_6\text{O}_{24}\text{H}_6]^{3-}@NU-1000$ and $[\text{CoMo}_6\text{S}_{12}\text{H}_{12}]^{4-}@NU-1000$ are confined in orientation-specific fashion within the size matching c-pore (1 nm) of hierarchically porous MOF NU-1000 in figure 4.2. Of these the $[\text{RhMo}_6\text{O}_{24}\text{H}_6]^{n-}@NU-1000$ was found to be active for CO oxidation and the $[\text{CoMo}_6\text{S}_{12}\text{H}_{12}]^{4-}@NU-1000$ for the HER reaction. Self-limiting loading of one cluster per pore, and associated nano-confinement, serve to isolate each POM and prevent consolidation by sintering.

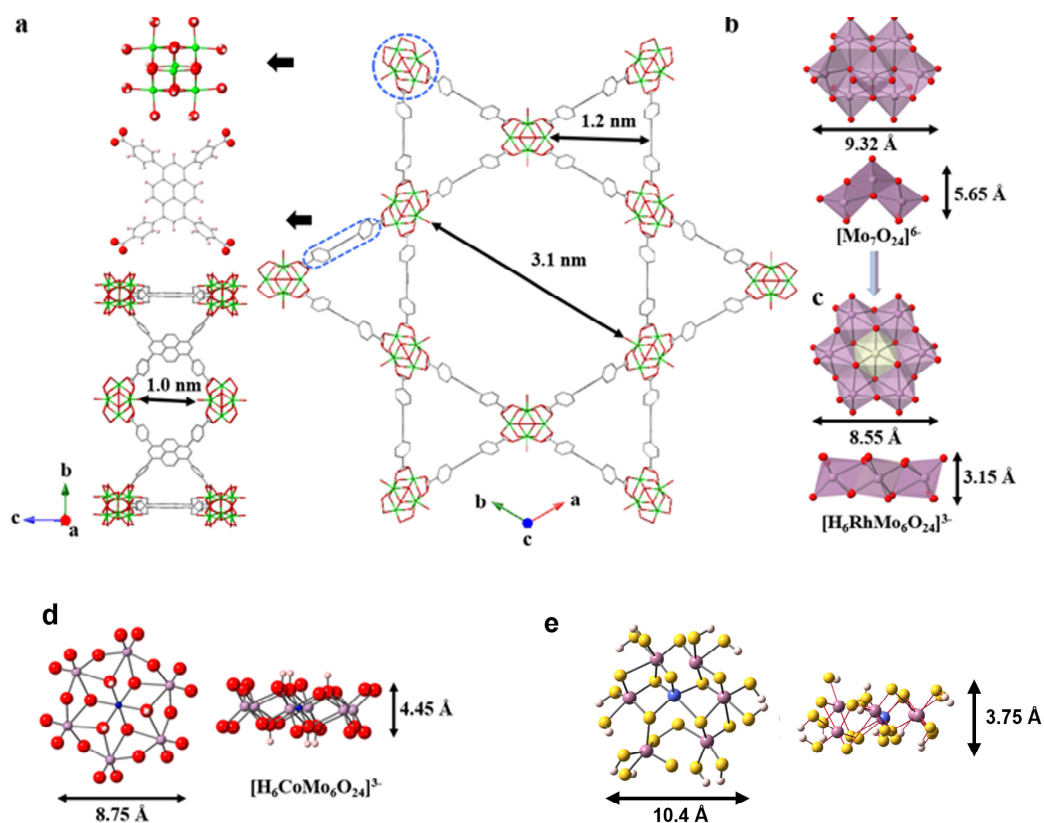


Figure 4.2: (a) Crystal structure of NU-1000, showing the 3.1 nm and 12 nm channels. Each layer is separated by 1.0 nm windows. The structures for the nodes and linkers are given. Polyhedral representation and size of (b) $[\text{Mo}_7\text{O}_{24}\text{H}_6]^{6-}$ and (c) $[\text{RhMo}_6\text{O}_{24}\text{H}_6]^{3-}$ seen from the top and side and molecular representation and size of (d) $[\text{CoMo}_6\text{O}_{24}\text{H}_6]^{3-}$ and (e) $[\text{CoMo}_6\text{S}_{12}\text{H}_{12}]^{4-}$ seen from the top and side. C= gray, Zr= green, H= white, O= red, Mo= purple, Rh= light green, Co= blue, S= yellow

4.1.3 Challenges in determining the active site structure

Since Anderson POMs supported in NU-1000 have not been synthesized before the exact composition and structure of the active site is not known. To corroborate the experimental data and understand the structure of the active site, simulations are an invaluable tool. We simulated several candidate computational models for the active site of $\text{RhMo}_6\text{O}_{24}$ @NU1000 and the sulfided Anderson POM $\text{CoMo}_6\text{S}_{24}$ @NU-1000. These were then compared to the experimental characterization data to elucidate the structure of the active site. This helped us understand the structure of the catalyst that rationalized the activity of these catalysts .

4.2 Experimental Methods and Results

Our experimental collaborators synthesized and characterized these catalysts. Direct impregnation is used to install $\text{RhMo}_6\text{O}_{24}\text{H}_6$, $\text{Mo}_7\text{O}_{24}\text{H}_6$ and $\text{CoMo}_6\text{O}_{24}$ in NU-1000. Synchrotron-based X-ray scattering methods, together with other spectroscopic methods, were used to establish the framework siting and corroborate the structure of the catalyst and its support. More details on the experimental methods are given in this paper [113]. Below I will briefly summarize the experimental results that were directly compared with simulations.

4.2.1 $\text{RhMo}_6\text{O}_{24}$ @NU-1000 catalyst

To assess if the $\text{RhMo}_6\text{O}_{24}\text{H}_6$ @NU1000 was encapsulated in NU-1000 *in-situ* and fully accessible to CO, diffuse reflectance infrared fourier transform spectroscopy (DRIFTS) was carried out. This technique is useful in also determining the presence of a single rhodium atom or a cluster. $\text{RhMo}_6\text{O}_{24}\text{H}_6$ @NU1000 and unsupported

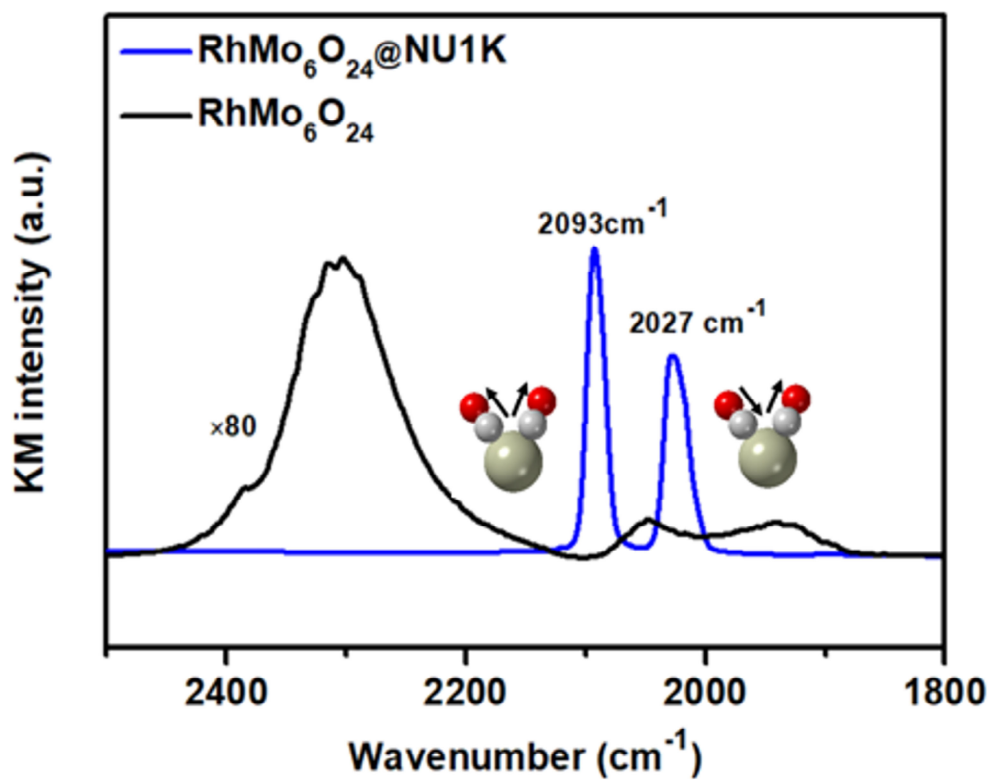


Figure 4.3: DRIFT spectra of CO adsorption on the unsupported RhMo₆O₂₄ and RhMo₆O₂₄@NU1000 catalysts at room temperature. Spectra were collected after CO adsorption to saturation and Ar purging. Catalyst exposed to CO showing two main characteristic CO vibrations.

$\text{RhMo}_6\text{O}_{24}\text{H}_6$ were exposed to CO and monitored by DRIFTS. For $\text{RhMo}_6\text{O}_{24}\text{H}_6@NU1000$ exposure yields prominent peaks at approximately 2093 and 2027 cm^{-1} that are attributed to the symmetric and asymmetric vibrations, respectively, of gem-dicarbonyl Rh(I) [116] (figure 4.3). Notably absent are peaks due to bridged CO (1860 cm^{-1}) thus ruling out the formation of Rh clusters and indicating the preservation of the catalyst as single Rhodium atom [117]. In contrast, non-porous, low surface area unsupported $\text{RhMo}_6\text{O}_{24}\text{H}_6$ (black line in figure 4.3) registers almost no response to CO and in particular no indication of gem-dicarbonyl species.

4.2.2 $\text{CoMo}_6\text{S}_{24}@NU-1000$ catalyst

The $\text{CoMo}_6\text{O}_{24}$ was synthesized and confined within the c-pores of NU-1000 via annealing; we refer to this structure as $\text{CoMo}_6\text{O}_{24}@NU-1000$. The cluster is sulfonated by heating under H_2S [37, 118], which functions as the source of sulfur and also as a reductant for converting Mo(VI) primarily to Mo(IV) to synthesize $\text{CoMo}_6\text{S}_{24}@NU-1000$. The isolated $\text{CoMo}_6\text{S}_{24}@NU-1000$ sizes are ~ 1.0 nm, and the structures expose abundant active S edge sites. Structural characterization with XAFS and XRD data provided the information in table 4.1. The X-ray Diffraction (XRD) technique was used to generate the differential probability pair distribution function (dPDF) [119] spectra of the bond-lengths with details in this paper [114]. The dPDF spectra of bond lengths is given in figure 4.4 where the peak positions correspond to different atomic distances within the POM cluster. The dPDFs are differential because the bare NU-1000 is subtracted in order to provide structural information for the cluster.

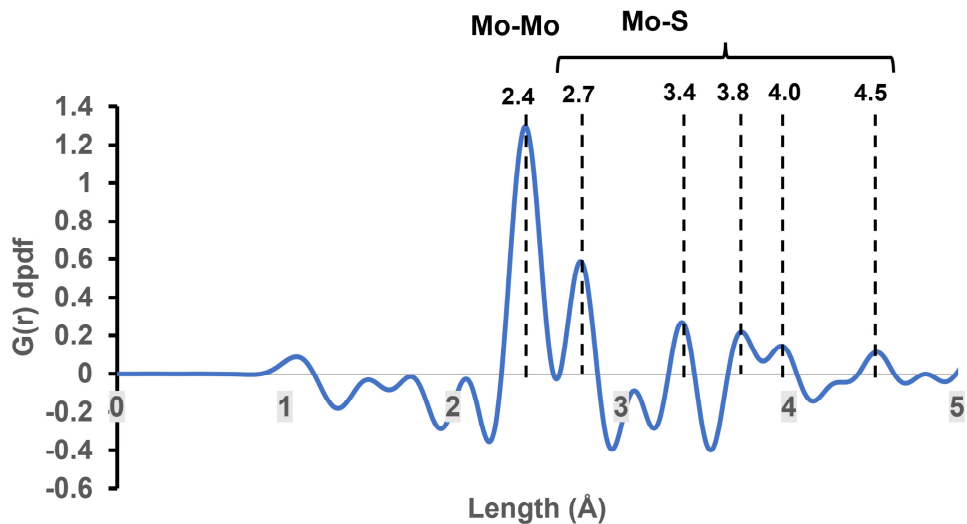


Figure 4.4: Experimental dPDF of the $\text{CoMo}_6\text{S}_{24}@NU-1000$ catalyst from XRD.

Property	$\text{CoMo}_6\text{S}_x\text{H}_x @NU1000$
Mo oxidation state	+4.0
Co oxidation state	+2.0
S/Mo ratio	3.85
Mo/Co ratio	6.0

Table 4.1: Structural information from experimental data for the $\text{CoMo}_6\text{S}_{24}@NU1000$ catalyst

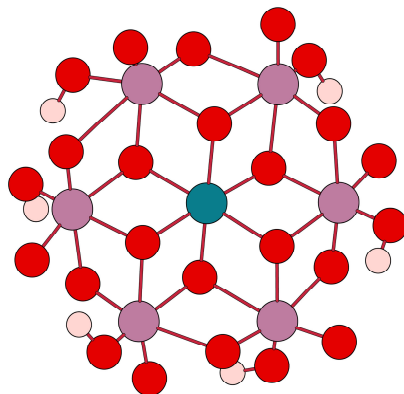


Figure 4.5: $[\text{RhMo}_6\text{O}_{24}\text{H}_6]^{3-}$ structure. C=gray, H= white, O=red, Mo=purple, Rh=blue

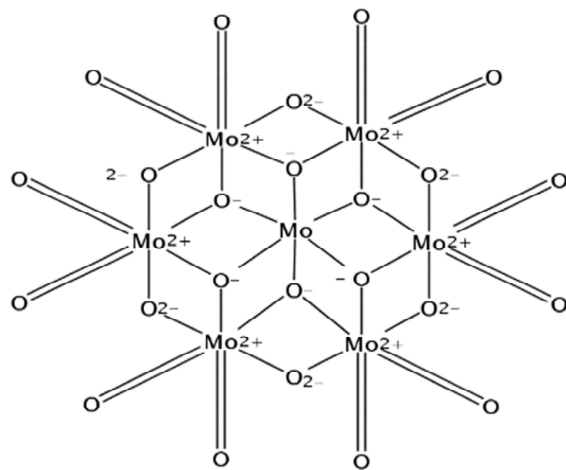


Figure 4.6: $[\text{Mo}_7\text{O}_{24}]^{6-}$ structure obtained from the CAS database registry Number 126094-83-5

4.3 Computational Methods

Several structures for both catalysts were computed to compare with experimental characterization data. DFT simulations were carried out to compute the energies and frequencies of different candidate structures with the M06-L functional in Gaussian-09 (2.3.1). No atoms were fixed during geometry optimization of the cluster models.

To compare with experiment, different CO binding geometries were simulated, along with their vibrational modes. Several models of $\text{RhMo}_6\text{O}_{24}\text{@NU-1000}$ catalyst when exposed to CO are computed by DFT calculations. It is expected that there will be two peaks due to the CO molecules in the frequency computations corresponding to the peaks in the DRIFTS with one being symmetric and the other being anti-symmetric. This is to determine that the Rh is indeed a single site as opposed to a metallic cluster. Starting from the $[\text{RhMo}_6\text{O}_{24}\text{H}_6]^{3-}$ structure (figure 4.5) two oxygen atoms were removed and replaced with two CO molecules. Four structures models were computed: model 1 with composition $\text{RhMo}_6\text{O}_{22}\text{H}_6(\text{CO})_2]^{3-}$, model 2 with composition $\text{RhMo}_6\text{O}_{22}\text{H}_9(\text{CO})_2$, model 3 $[\text{RhMo}_6\text{O}_{22}\text{H}_6(\text{CO})_2]^{1-}$ and model 4 $\text{RhMo}_6\text{O}_{22}\text{H}_7(\text{CO})_2$. Rh is in +3 oxidation state in models 1 and 2 and in +1 oxidation state in models 3 and 4. Two spin states (singlet and triplet) of each structure models were evaluated.

To compare with experimental characterization data, sulfided $\text{CoMo}_6\text{S}_{24}\text{@NU-1000}$ structure was simulated. As fully sulfided analogues of the Anderson POM are unknown, we started from the structure of $[\text{Mo}_7\text{O}_{24}]^{6-}$ (figure 4.6) and replaced the central Mo atom with a Co atom and all O atoms with S atoms. We then varied the H and S contents, chemical states of S, and overall cluster charges and performed geometry relaxations in DFT. In all we evaluated over 90 structures. The final atomic

Structure	$[\text{RhMo}_6\text{O}_{22}(\text{CO})_2\text{H}_6]^{1-}$	$[\text{RhMo}_6\text{O}_{22}(\text{CO})_2\text{H}_7]$	Experimental
Singlet	2051 cm^{-1} , 2115 cm^{-1}	2060 cm^{-1} , 2124 cm^{-1}	2027 cm^{-1} , 2093 cm^{-1}
Triplet	2012 cm^{-1} , 2056 cm^{-1}	2102 cm^{-1} , 2150 cm^{-1}	

Table 4.2: Scaled IR Frequencies by 0.976 of the computed structures of the $[\text{RhMo}_6\text{O}_{22}\text{H}_6(\text{CO})_2]^{1-}$ and $\text{RhMoO}_6\text{O}_{22}\text{H}_7(\text{CO})_2$ with different spin states and the experimental values

coordinates were analyzed by generating the dPDF spectra [120] of the computed structures and comparing them with experimental dPDF from XRD data.

4.4 Results and Discussion

4.4.1 Active Site Structure of $\text{RhMo}_6\text{O}_{24}@\text{NU-1000}$ catalyst

It was found that the computed vibrational frequencies of CO in models 3 ($[\text{RhMo}_6\text{O}_{22}\text{H}_6(\text{CO})_2]^{1-}$) and 4 ($\text{RhMoO}_6\text{O}_{22}\text{H}_7(\text{CO})_2$) with Rh in +1 oxidation state (figure 4.7 and table 4.2) are in much better agreement with experiments (2027 cm^{-1} , 2093 cm^{-1}). The models 1 and 2 with Rh in +3 oxidation state had lower frequencies than experiments. The singlet structures (low spin) are also the lowest energy similar to previous works [116, 121] on single atom Rh catalysts. They are slightly higher than the experimental values possibly due to the error from approximations used in the DFT functional. The $[\text{RhMo}_6\text{O}_{24}\text{H}_6]^{1-}$ and $[\text{RhMo}_6\text{O}_{24}\text{H}_7]$ give very similar symmetric (2051 cm^{-1} , 2061 cm^{-1}), and anti-symmetric frequencies (2115 cm^{-1} , 2124 cm^{-1}) in line with what is expected of the supported single atom Rhodium dicarbonyl $\text{Rh}(\text{CO})_2$ [121, 122, 123]. Hence singlet structures of the models 3 and 4 shown in figure 4.7 are representative of the experimentally synthesized catalyst with a single Rh atom surrounded by Mo and O atoms.

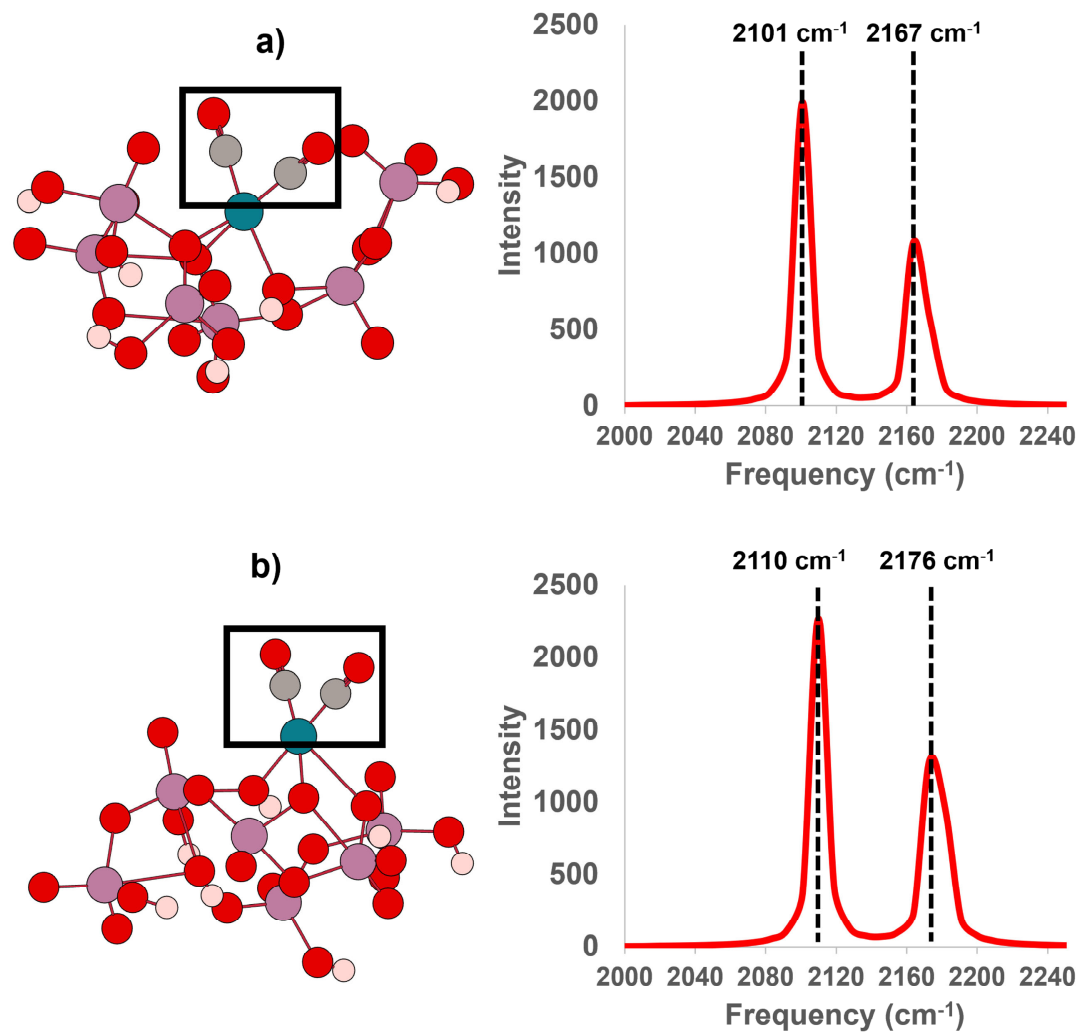


Figure 4.7: Representation of two catalysts models a) $[\text{RhMo}_6\text{O}_{22}(\text{CO})_2\text{H}_6]^{1-}$ and b) $\text{RhMo}_6\text{O}_{22}(\text{CO})_2\text{H}_7$ with their corresponding IR spectrum from Gaussian-09 C=gray, H= white, O=red, Mo=purple, Rh=blue

4.4.2 Active Site Structure of $\text{CoMo}_6\text{S}_{24}$ @NU-1000 catalyst

Initially it was hypothesized by our experimental collaborators that the S_2^{2-} terminal groups exist that catalyze the HER reaction. To verify this hypothesis, we started from the structure (figure 4.6) and replacing all O atoms with S atoms and the central atom with Co, a base structure was optimized. 90 different variations of this structure were computed and compared by short (bond lengths 1.8-3.0 Å) and long (bond lengths 1.8-5.0 Å) pearson correlation with the experimental dPDF. The short correlation has two peaks i.e. the Mo-Mo at ~ 2.4 and Mo-S at ~ 2.7 that are the most relevant to the analysis as at longer bond lengths there is less certainty in assigning them to specific atom pairs. The general observations and inferences from the comparison of computed structures with the experimental results are enumerated below.

1. Clusters models with overall negative charge exhibit bond lengths in better agreement with dPDF than neutral and positively charged clusters. Representative neutral (figure 4.8a) and positively charged (figure 4.8b) models with low short pearson correlations 63% and 81% respectively illustrate this point.
2. To simulate the S/Mo ratio of less than 4 (experimental is 3.83), we attempted to substitute one of the sulfur atoms with an oxygen atom in order to vary the S to Mo ratio, but doing this results in Mo-S bond lengths that give less agreement with experiment in the dPDFs (figure 4.8 c and d). This indicates that the lower S to Mo ratio can be attributed to removal of a S atom creating a coordinately unsaturated Mo site that can take part in the HER reaction. A representative structure that agrees well with experimental dPDF data is given in figure 4.9.

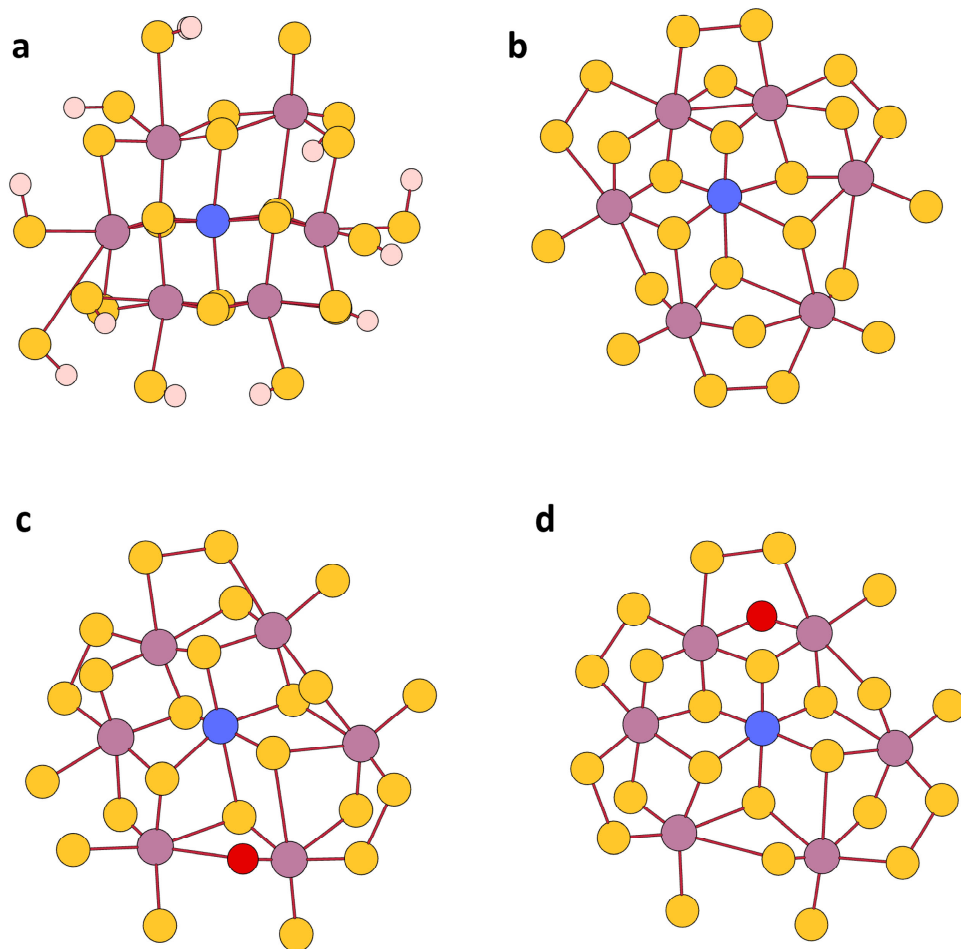


Figure 4.8: Example of structures that are a) uncharged with formula $[\text{CoMo}_6\text{S}_{12}\text{H}_{12}]^0$ with 63% short and 54% long pearson correlation and b) positively charged with formula $[\text{CoMo}_6\text{S}_{24}]^{2+}$ with of 81% short and 65% long pearson correlation c) an oxygen substituted configuration with formula $[\text{CoMo}_6\text{S}_{23}\text{O}]^0$ with 81% short and 65% long pearson correlation and d) another oxygen substituted configuration positively charged with formula $[\text{CoMo}_6\text{S}_{23}\text{O}]^0$ with 83% short and 66% long pearson correlation. C=gray, H= white, S=yellow, O= red, Mo=purple, Co=blue

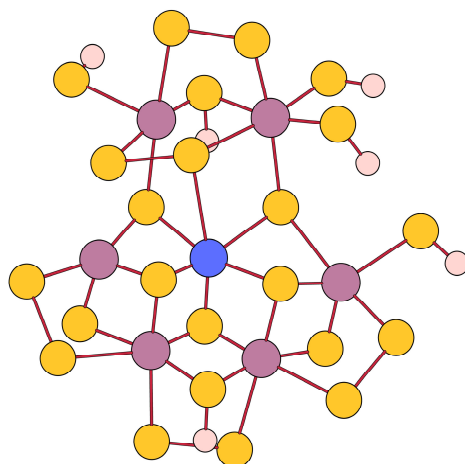


Figure 4.9: a) $[\text{CoMo}_6\text{S}_{12}\text{H}_{12}]^{4-}$ with 87.9 % short and 78.4% long pearson correlation C=gray, H= white, S=yellow, Mo=purple, Co=blue

3. For structures containing hydrogen, the hydrogen atoms prefer binding to S to form sulfhydryl ligands. While often terminal, these sulfhydryl ligands can sometimes be bridging. Structures comprising H_2S ligands in general gave less agreement with dPDF. All structures computed structures with their pearson correlations are given in this repository [124].
4. Structures where Mo has a coordination number of 6 exhibit bond lengths that agree well with dPDF. The coordination number of 6 also agrees with XAS results (table 4.1).
5. The structure that matches 93% (short pearson correlation) with experimental dPDF data is charged by 4- and a high spin octet (shown in figure 4.10). The structure contains SH groups in the peripheral/terminal groups and has the chemical formula $[\text{CoMo}_6\text{S}_{12}\text{H}_{12}]^{4-}$

Based on this structure we hypothesized that the terminal S atoms were hy-

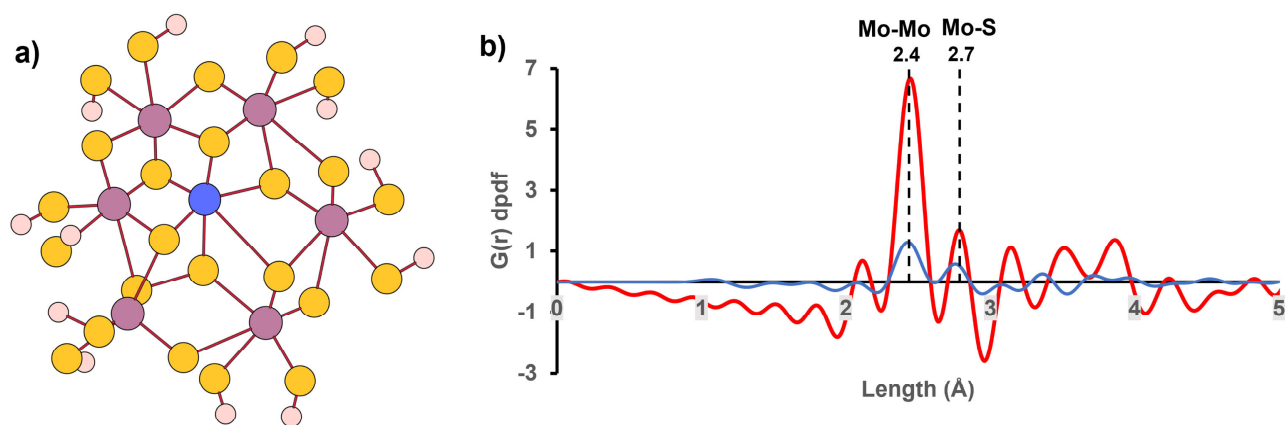


Figure 4.10: a) $[\text{CoMo}_6\text{S}_{12}\text{H}_{12}]^{4-}$ (octet spin state) with 93% short and 80% long pearson correlation b) dpdf of the bond lengths for red = computational structure blue = experimental

drogenated to SH groups upon exposure to hydrogen during HER reaction, which is why the dominant structure has SH groups. Since the catalyst has slightly lower S/Mo ratio of 3.8, it indicates the possibility that some of these SH groups leave to create a coordinatively unsaturated site that catalyzed the HER. Since there could be a number of such structures and evaluating all possible combinations would have led to large computational expense, a representative structure that agrees reasonably well with the dPDF data (figure 4.9) is proposed.

4.5 Conclusions

Computational modeling corroborates the experimental structure characterization data of Anderson POM@NU-1000 catalysts ($\text{RhMo}_6\text{O}_{24}$ @NU-1000 and $[\text{CoMo}_6\text{S}_{12}\text{H}_{12}]^{4-}$ @NU-1000). For the $\text{RhMo}_6\text{O}_{24}$ @NU-1000 catalyst the proposed low spin (singlet) models $[\text{RhMo}_6\text{O}_{22}\text{H}_6(\text{CO})_2]^{1-}$ and $\text{RhMo}_6\text{O}_{22}\text{H}_7(\text{CO})_2$ matches the experimental DRIFTS, also confirming the gem Rh(I) as the active site for CO oxidation reactions. This structure can be used for developing a reaction kinetic model to compute the energetics of reaction. Contrary to the initial hypothesis, it appears that the $\text{CoMo}_6\text{S}_{24}$ @NU-1000 cluster has SH as terminal groups with chemical composition $[\text{CoMo}_6\text{S}_{12}\text{H}_{12}]^{4-}$ @NU-1000, instead of S_2^{2-} groups that in combination with Mo catalyze HER. This is a unique insight provided from modeling. It also indicates the possibility that SH atoms can be removed from the cluster to create more un-coordinated sites for reaction. Using this information, a more reduced cluster (Mo_7S_{17}) with lower S/Mo ratio atoms was synthesized that increases the number of uncoordinated sites on Mo atoms and was active for the more challenging hydrogenation of acetylene.

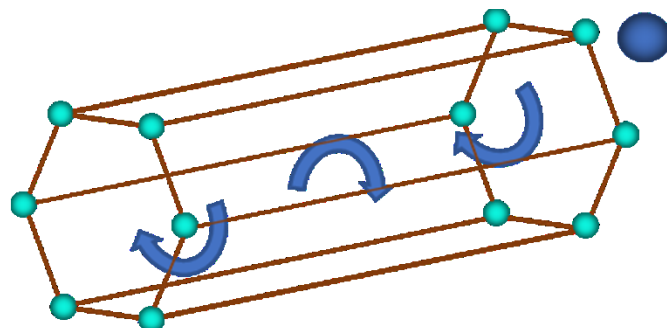
Chapter 5

Analyzing choices in microkinetic modeling

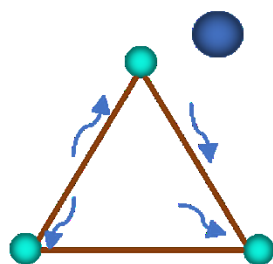
5.1 Introduction

As demonstrated in chapter 3 microkinetic modeling is a tool to identify the dominant reaction mechanism and rate determining steps to gain mechanistic understanding of catalysis. It also incorporates the impact of temperature, pressure and concentration of reactants and products on the rate constants. There are many sources of uncertainty in microkinetic models particularly related to: the choice of DFT functional [125], harmonic approximation [126], model of active site and reaction mechanism [127]. In addition, the guest species in MOFs have complex diffusive behavior due to structural anisotropic pores that requires more elaborate modeling techniques. In this chapter we will analyze the adsorption models, DFT functionals and catalyst models to understand their impact on results of microkinetic modeling.

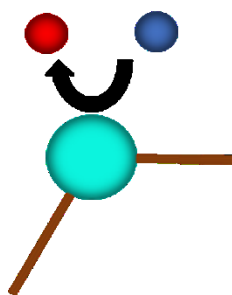
A microkinetic model takes as input a guess of the reaction mechanism, the calculated energetics, and a strategy for how to compute the rate constants (specifically,



Large pore: Minimal host-guest interactions, transport via Knudsen diffusion



Small pore: Significant host-guest interactions influence molecule transport



Catalytically active site: Strong host-guest interactions limit molecule transport

● reactant
 ● product
 — MOF Linker
 ● Metal Center

Figure 5.1: Different types of molecule transport in MOFs are determined by host-guest interactions

the pre-exponential terms) [46]. For a simple catalytic system, e.g., a uniform flat surface, these terms are calculated using transition state theory for surface reactions and collision theory for adsorption reactions [44, 128] as done in chapter 3.

Collision theory assumes that the gas phase is ideal with each molecule possessing full translational, rotational, and vibrational degrees of freedom and that impingement onto the surface results in a loss of one translational degree of freedom. MOFs exhibit various modes of transport [129, 130, 131, 132, 133, 134] as shown in figure 5.1. The collision theory model for adsorption is likely inaccurate for MOFs due to host-guest interactions which put guest molecules in close contact with the pore walls and each other [135], leading to interacting groups of molecules that transport via diffusion like in a liquid. In some cases, this issue can likely be resolved by replacing collision theory-based pre-exponential terms in a kinetic model with rate constants based on diffusion theory. For example, diffusion in large-pore MOFs is modeled using Knudsen theory, which is similar to collision theory but accounts for collisions with the surface of the MOF pore. While this can be a good approximation, in case of NU-1000 the diffusion coefficient determined from Knudsen theory is an order of magnitude higher than the diffusion coefficient determined from atomistic simulations [74]. Based on this, we want to determine rate constants derived from atomistic molecular dynamics simulations to improve upon our previous adsorption model from collision theory. We want to combine this with microkinetic modeling which to our knowledge has not been done before in MOFs.

To ascertain how the variability in microkinetic modeling results depend on the choice of DFT functional, catalyst and adsorption models, we have chosen ethene dimerization on a Ni catalyst supported on NU-1000 as a test reaction (figure 5.2). We have addressed these questions by evaluating the predicted rates from the microkinetic modeling from two DFT functionals (M06-L and PBE), and two models of active site

(cluster and periodic). We also perform molecular dynamics simulations to get an estimate of the adsorption rate constants.

5.2 Computational Methods

5.2.1 DFT Calculations

DFT calculations were performed on the cluster (figure 2.2) and periodic models (figure 2.1) to get the energies of reaction intermediates and transition states for ethene dimerization reaction (figure 5.2). The cluster model is the same as used in chapter 3. Two DFT exchange-correlation (XC) functionals the M06-L and the PBE are used to calculate the energies. Further details are in section 2.3.1. The PBE DFT functional was used for periodic calculations (section 2.3.2) on the model (figure 2.1).

5.2.2 Microkinetic Modeling

Microkinetic models are run over temperature ranges of 50-200°C. The total pressure is set to atmospheric and comprises 100% ethene. All pressures are held constant over the course of simulation. Since butene is not introduced into the system, this represents the case where the % conversion of ethene equals zero. Each simulation is run for 10^8 s and considered to be converged when the changes in the fractional concentrations of all of the reaction intermediates between successive iterations are less than 10^{-12} . Adsorption (k_{ads}) desorption (k_{des}) and activated (k_{des}) rate constants are calculated as detailed in section 3.2.2.3. Partition functions are calculated with TAMkin (section 2.3.3). Another microkinetic python solver was also developed that has the flexibility to incorporate custom adsorption and desorption rate constants [136].

5.2.3 MD Calculations

MD simulations were performed to get an estimate of the probability of ethene forming a bond with the Ni catalyst at 300 K and 1 atm. The details of the force-field parameters for the MD simulations are detailed in sections 2.3.4 and 2.3.6. The simulation box was the same as the unit cell of NU-1000 given in figure 2.1. One ethene molecule was introduced into the system and allowed to be mobile with the rest of the framework atoms fixed. 10 trajectories of 16 nanoseconds were generated each starting from different configurations of ethene molecule. Center-of-mass coordinates for each molecule were extracted from the simulation every 160 femtoseconds corresponding to h/k_bT femtoseconds (h =planck's constant, k_b =Boltzmann's constant and $T = 300$ K) in this case. The temperature and energy were monitored to make sure that there were no major fluctuations during the runs.

5.2.4 AIMD Calculations

The AIMD simulations were run to capture the correct interaction near Ni modeled by DFT calculations and MD simulations detailed in section 2.3.7. The simulations were run for anywhere between 300-1000 femtoseconds starting with four different configurations for ethene to examine the specific configurations of adsorption.

5.2.5 GCMC Calculations

To determine the number of ethene molecules in the unit cell of NU-1000 at specific temperature and pressure conditions, GCMC simulations are performed (section 2.3.5). This is to correct the results of MD simulations with one ethene molecule. The conditions considered are 4 temperatures (25° C, 45° C, 75° C and 200 ° C) and 3 pressures (1, 2 and 10 atm) at 100% ethene concentration.

5.3 Results and Discussion

5.3.1 Catalyst Models and DFT Functionals

To understand the impact of catalyst models and DFT functionals, reaction energies and activation barriers were calculated for the cluster models with DFT functionals PBE and M06-L and the periodic model with functional PBE for the Cossee-Arlman (CA) mechanism of ethene dimerization (figure 5.2). The periodic model has ~ 570 atoms with full linkers and Zirconium nodes and a gaussian and planewave basis set. The cluster model has ~ 70 atoms with one Zr node and linkers truncated as carboxylate groups and a gaussian basis set. These were input into the microkinetic model as detailed in section 3.2.2.3 to get the rate of ethene dimerization that is plotted versus temperature in figure 5.4. The energies of desorption of adsorption/desorption reaction (rxns 1, 3 and 6) and activation barriers of activated reaction steps (rxns 2, 4 and 5) are shown in figure 5.4.

5.3.1.1 Cossee-Arlman (CA) Mechanism for Ethene Dimerization

We are using ethene dimerization on NU-1000 as a test reaction. Previous work with DFT and multi-reference calculations [24] has shown that the Cossee-Arlman (CA) mechanism (figure 5.2) is energetically favorable as compared to other mechanisms on this catalyst. In the CA mechanism the active site is a metal hydride. Ethene C_2H_4 (g) adsorbs to the active site (rxn-1 figure 5.2) and then reacts with the metal hydride, forming an ethyl moiety, C_2H_5 (rxn-2 figure 5.2). Another C_2H_4 (g) molecule adsorbs to the active site (rxn-3 figure 5.2) and reacts with C_2H_5 to form C_4H_9 in a C-H bond formation step (rxn-4 figure 5.2). The C_4H_9 moiety goes through transition state (rxn-5 figure 5.2) to form adsorbed C_4H_8 which then desorbs (rxn-6 figure 5.2) to regenerate the metal hydride.

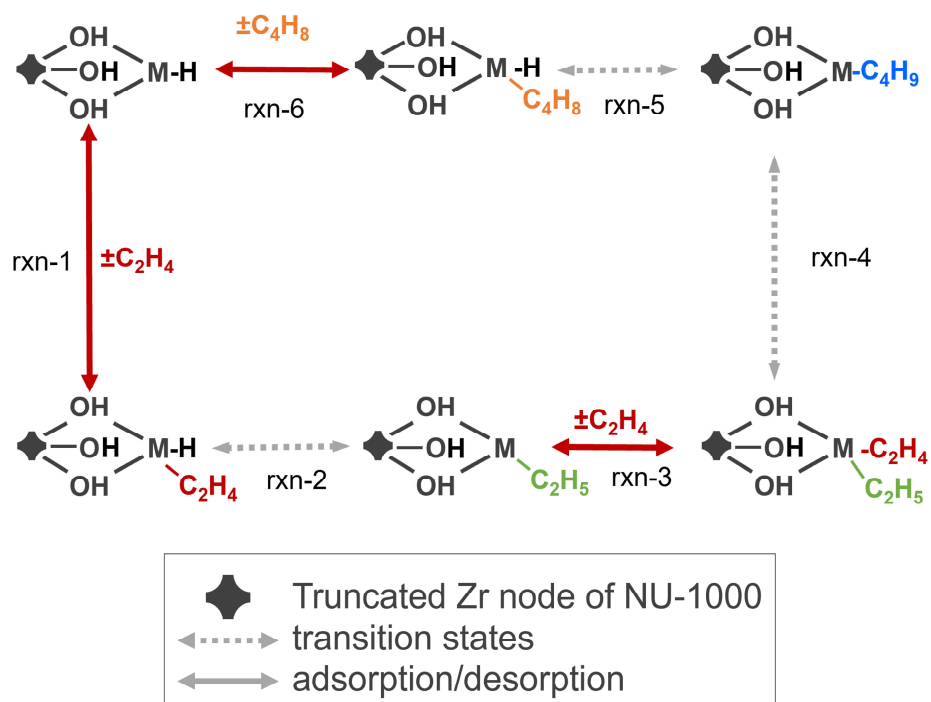


Figure 5.2: Cossee-Arlman Mechanism of Ethene dimerization on NU-1000 catalyst

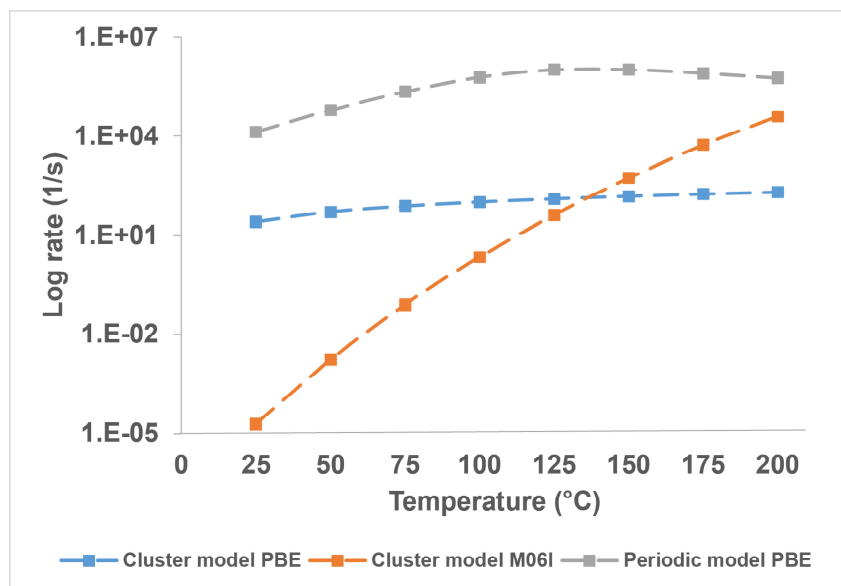


Figure 5.3: Comparing the difference in rates for the model in the truncated cluster Gaussian 09 (M06-L and PBE functionals) periodic CP2K models

5.3.1.2 PBE functional with cluster and periodic catalyst models

With the the same functional (PBE) in both periodic and cluster models the shape of the plots is similar yet there is a three order of magnitude difference in the rates they predict (figure 5.3). The difference in the models can be due to the presence of linkers and different basis sets as both factors can impact the energies of calculated reaction steps and its difficult to separate these effects. Examining the energetics of the reactions, there is a much larger difference in adsorption energies (figure 5.4a) than the activation energies (figure 5.4b). For the periodic model, the rate is high initially due to high C_2H_4 adsorption energy (-164 kJ/mol) in rxn-1 that becomes limited by lower adsorption energy (-65 kJ/mol) in rxn-3 at higher temperatures (figure 5.4a). This is due to the stabilizing influence of linkers when C_2H_4 adsorbs to the Ni hydride in rxn-1. For the cluster model, the reaction is limited by the unfavorable adsorption

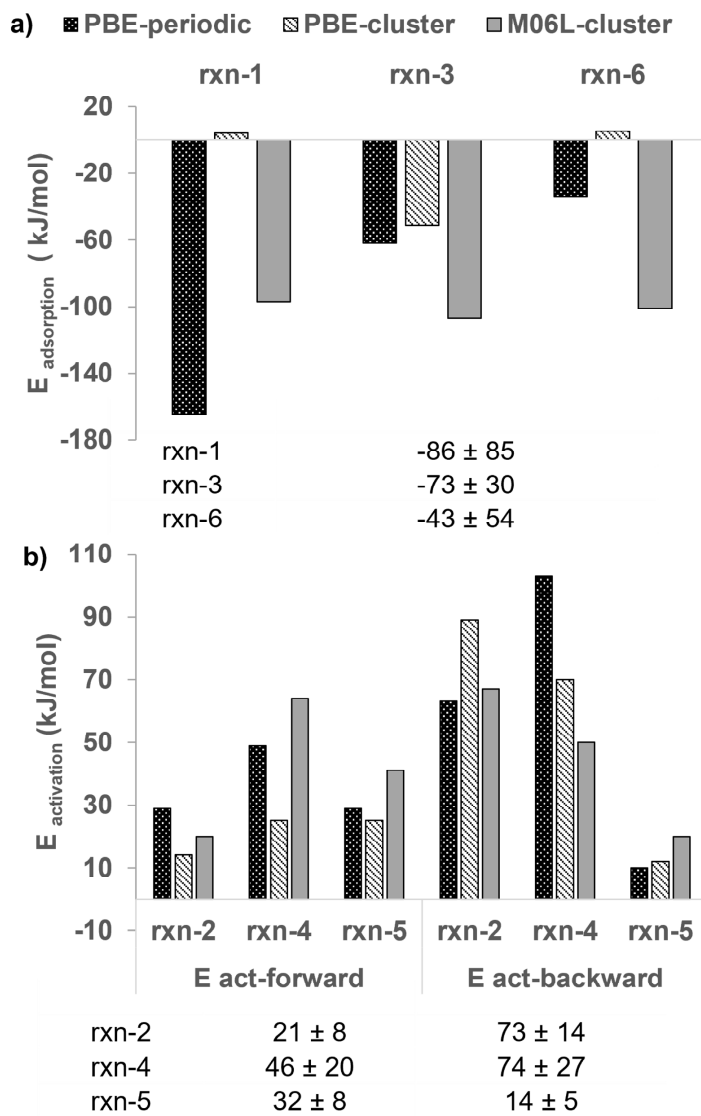


Figure 5.4: Truncated cluster Gaussian 09 (M06-L and PBE functionals) and periodic CP2K models (PBE functional) a) Desorption energies b) forward and backward activation energies with tabulated mean and standard deviation values

of C_2H_4 in rxn-1 (adsorption energy = 4 kJ/mol). There are differences in these models based on the number of atoms and the basis set used which could contribute to the differences in energy, nevertheless it is important to note that the choice of XC functional is not the only significant source of variation in these models.

5.3.1.3 PBE and M06-L functionals with cluster model

To eliminate the variance due to the model and basis set, the microkinetic modeling rates for the cluster models with the functionals PBE and M06-L are compared (figure 5.3). There is still a significant difference in the shape and the order of magnitude in rates. For M06-L, the adsorption energies are comparable to each other for all three steps. Here the forward reaction barrier for rxn-4 (figure 5.4b) is controlling the rate of reaction that decreases as the temperature is increasing. For PBE, the reaction is limited by the unfavorable adsorption of C_2H_4 (g) in rxn-1 as evidenced by positive adsorption energies, that limits the increase in reaction rate at high temperatures as adsorption becomes even more unfavorable. All three models predict activation energies with much less standard deviation from the mean value as compared to the desorption energies. The energy with the largest spread is the ethene desorption energy of rxn-1 (86 +/-85).

5.3.2 Impact of adsorption models

5.3.2.1 Rate of adsorption vs rate of dimerization

As shown in the previous section, the energies of adsorption have a significant impact on the rate of ethene adsorption with changing temperatures with respect to its shape as well as order of magnitude of overall rates. The rate of adsorption can be varied by changing the adsorption energies and the pre-exponential factor. The colli-

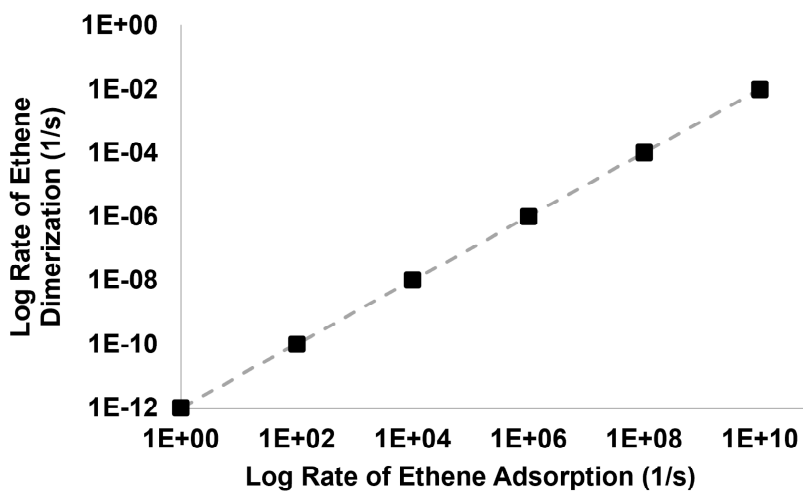


Figure 5.5: Variation in adsorption rate of 100% ethene versus the ethene dimerization rate at $T = 300$ K, $P = 1$ atm

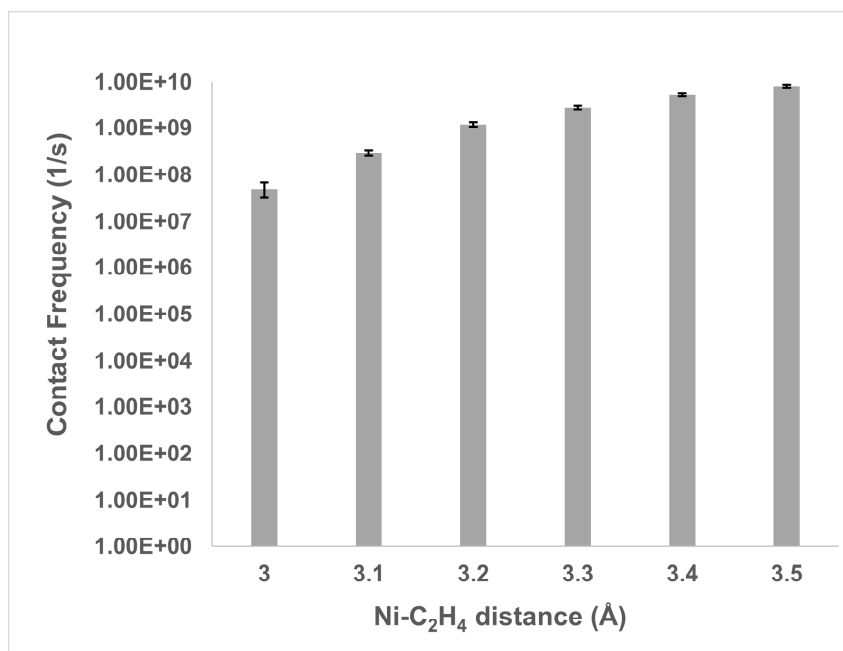


Figure 5.6: Contact frequency of C₂H₄ with Ni versus the Ni to C₂H₄ distances

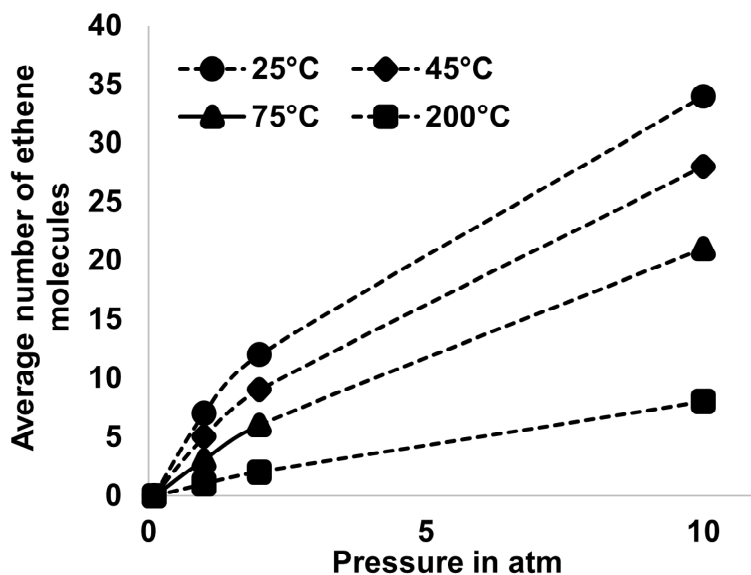


Figure 5.7: Adsorption Isotherms generated from GCMC simulations

sion theory calculates the rate of adsorption by $k_{ads} = \frac{yPA}{\sqrt{2\pi mk_b T}}$ and rate of desorption by $k_{des} = \frac{k_b T^3}{h} \frac{A(2\pi mk_b T^3)}{\sigma \Theta_{rot}} e^{\frac{-E_{des}}{k_b T}}$ (equation 1 and 2 in section 3.2.2.3). By changing the rate of ethene adsorption (rxn-1) without changing the E_{des} , a microkinetic model (section 3.2.2.3) with energies from the periodic PBE CP2K model (section 2.1) is simulated. Varying the rate of adsorption spanning 10 to 10^{10} (1/s) while the rest of the parameters are held constant, gives a direct proportionality between rates of ethene adsorption and dimerization (figure 5.5). For reference the rate of adsorption calculated from collision theory model (3.2.2.3) is in the order of 10^8 at the conditions of 300 K, 1 atm and 100% ethene. This illustrates that if collision theory is not the correct model for adsorption, there could be orders of magnitude difference in overall rates.

5.3.2.2 Rate of Adsorption from MD simulations

To verify the validity of the rate determined from collision theory, an alternate method is explored. MD simulations (details in section 5.2) were run for a single ethene molecule in unit cell of Ni-NU-1000. The contact frequency of C_2H_4 (g) molecule with the Ni atom is plotted for the Ni to C_2H_4 distances in figure 5.6. Here a ‘contact’ is defined as instances of when two or more consecutive samples each (taken at 160 femtoseconds) are within the distance specified. This contact number is divided by the total simulation times to get the ‘contact frequency’. Each data point in this plot is averaged over ten trajectories. The error bars represent the standard error within samples.

To analyze the impact of temperature and pressure on the number of ethene molecules in the unit cell of NU-1000 we did GCMC simulations (figure 5.7). Corresponding to the conditions we are interested in (1 atm and 300 K at 100% ethene), the unit cell of NU-1000 contains 6 to 7 ethene molecules. Multiplying this with our contact frequency for MD simulations does not change the order of magnitude so the analysis from MD simulations is valid.

If we assume that this contact frequency is roughly equivalent to the rate of ethene adsorption, the contact frequency that corresponds to the rate of ethene adsorption from collision theory (10^8) is at a cut-off distance of 3.1 Å between Ni and C_2H_4 (g) molecule. Since the force-field used in the MD model only accounts for the non-bonded Lennard-Jones (LJ) interactions, it is not able to capture the correct physical behaviour due to the strong coulombic attractive forces between Ni and C_2H_4 (g) molecule at distances approximately ≤ 3.5 Å. The MD simulations give us a rough idea of the order of magnitude of frequency of collisions due to LJ interactions between framework atoms and ethene molecule, but cannot capture the

physical behaviour of bonding near the vicinity of Ni atom.

5.3.2.3 Rate of Adsorption from AIMD simulations

To analyze the adsorption behaviour of the ethene molecule as it comes nearer than 3.5 Å, ab-initio molecular dynamics simulations (section 2.3.7) were performed. Four starting configurations of C₂H₄ were constructed within 5 Å of the Ni atom at different angles (figure 5.8). Examining the trajectories showed that there is a very specific head-on configuration of ethene that results in bonding of the molecule on the Ni catalyst (figure 5.8a). The trajectories starting from configurations b, c and d have the ethene molecule change its orientation to the specific configuration of a, before binding at a distance of 1.9 Å. If we can calculate the exact proportion of ethene molecules that come close enough in that specific orientation at the binding distance we can get a probability of binding for ethene. This requires developing a partitioning scheme with respect to distance. Here the challenge is to correctly determine the exact distance at which the Ni starts impacting the ethene molecule molecular path. The probability distribution of ethene contact frequency from MD simulations at that specific distance multiplied by the probability distribution from AIMD simulations will give a probability distribution of the adsorption rate constant. This is part of ongoing work.

5.4 Conclusions and Recommendations

In this chapter we have explored adsorption models, DFT functionals and catalyst models to understand their impact on results of microkinetic modeling. There is considerable variability in rates due to adsorption energies on the catalysts and not because of the activation barriers. In addition to variability due to the XC functional,

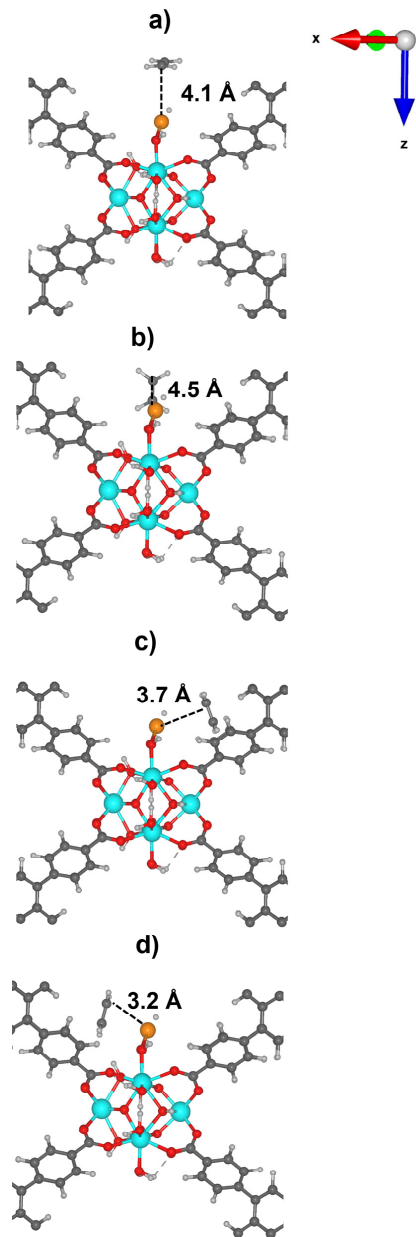


Figure 5.8: AIMD Configurations

DFT has limitations in predicting correct energies due to delocalization and self-interaction errors for which high level methods like configuration interaction (CI), perturbation theory (PT), and coupled cluster (CC) can be used. As these methods are very expensive for large systems like MOFs, a suggestion for future research is to use a partitioning scheme as shown by Rybicki and Sauer [137] in zeolites to tractably calculate the energies of these systems. As demonstrated in this chapter and from previous works [138] inaccuracies in the calculated energetics could lead to errors of several orders of magnitude in calculated reaction rate constants. We also addresses the validity of collision theory to model adsorption rate constant in MOFs, that could lead to erroneous results in ongoing work.

Chapter 6

Conclusions and Recommendations

6.1 Conclusions

In this dissertation, we have a) built models of active site of metal-oxo clusters in NU-1000, b) performed microkinetic modeling of metal cation catalysts in NU-1000 and c) analyzed the impact of modeling choices.

We calculated the reaction energetics for ethene hydrogenation and ethene dimerization in this work. For ethene hydrogenation the metal hydride active site and SW mechanism is shown to be not viable for all M@NU-1000 catalysts with a combination of high throughput reactor experiments, DFT calculations, and microkinetic modeling. We find that while valid for Ni@NU-1000, Cu@NU-1000, and Zn@NU-1000 catalysts, the metal hydride active site and SW mechanism are not valid for Mn@NU-1000, Fe@NU-1000, and Co@NU-1000 catalysts. The difference can be attributed to the spin state of the metal cation catalysts. Specifically, metal cations with low spin utilize a metal hydride active site and follow the SW mechanism, whereas metal cations with high spin utilize a bare metal cation active site and follow an alternate mechanism that employs proximal oxo groups for binding of

hydrogen species. The switch to the alternate from the SW mechanism is motivated by adsorption of H_2 , which becomes endergonic in the SW mechanism on high spin Mn@NU-1000, Fe@NU-1000, and Co@NU-1000. In contrast, H_2 adsorption is exergonic on Mn@NU-1000, Fe@NU-1000, and Co@NU-1000 catalysts in the alternate mechanism. We identified spin as an important design variable for C-H catalysis in 3d transition metals on MOFs. While there is orders of magnitude difference in the calculated and experimental rates, we have been able to replicate the trends in experimental rates with reasonable accuracy. The impact of different modeling choices is analyzed in order to compute the errors in the simulated rate for ethene dimerization. While this analysis is still ongoing there appears to be a larger uncertainty in the adsorption energies of the reactants and products than the activation barriers that's impacting the rates of the reaction.

We built a computational structural model corroborated by experimental structure characterization data for CO oxidation and HER catalysts supported in NU-1000. Here DFT is used with great success to elucidate the structure of the catalyst. The HER catalyst $[CoMo_6S_{12}H_{12}]^{4-}@NU-1000$, contrary to the initial hypothesis, appears to have SH as terminal groups, instead of S_2^{2-} groups that in combination with Mo catalyze HER. This is a unique insight provided from modeling. It also indicates the possibility that SH groups can be removed from the cluster to create more un-coordinated sites for reaction. Using this information, a more reduced cluster (Mo_7S_{17}) with lower S/Mo ratio atoms was synthesized that increases the number of uncoordinated sites on Mo atoms and was active for the more challenging hydrogenation of acetylene.

Overall, DFT has been used successfully to give interesting insights into kinetics and active site structure of MOF supported metal catalysts. Due to inherent flaws in DFT, there are certain aspects in MOF modeling that require high level QM methods. An important issue is incorporating confinement and configurational

effects of guest species in the framework. To address this we are in the process of incorporating dynamic methods into the microkinetic modeling.

6.2 Recommendations

The inferences and recommendations in the general context of MOFs have been summarized in our recently published perspective article [139]. I will shed light on some of these in the context of this dissertation specifically below.

The insights about the mechanism of C-H bond chemistry on M@NU-1000 catalysts in this work point to spin as a design variable. State-of-the-art multireference calculations are needed to accurately calculate the energetics of spin polarized metal cations [140, 141, 142]. Strategies that can tractably apply multiconfigurational methods to systems that incorporate framework effects are hence needed. QM/MM or “QM/QM” methods, which use more accurate wave function theory (WFT) methods to model the active site and DFT to incorporate longer range phenomena, may be particularly useful for such systems. For example, Cui and Schmidt [143] used QM/MM to compute activation barriers in zeolitic imidazolate frameworks (ZIFs) and achieved high accuracy and efficiency when compared to DFT. A future work recommendation is to develop and apply tractable methods for spin sensitive MOF systems. One can envision tuning activity and selectivity through spin, e.g., by varying the ligands, binding environments, supports, or metal cations, themselves. Further, these results point to partial pressure (e.g., of H₂) as possible “knob” for tuning catalytic activity. One can imagine tuning the H₂ pressure in order to convert a bare metal cation to a metal hydride or vice versa, hence altering the mechanism and rate of catalytic hydrogenation. There are clear opportunities for optimizing catalytic activity and selectivity on metal cation catalysts.

We have modeled the adsorption behaviour through MD simulations but cannot definitely say on the basis of current analysis if collision theory is indeed the correct model of adsorption in MOFs. An issue with the method we have used is that the force fields in MOFs that are used are commonly trained on relatively weak physical interactions, whereas host-guest interactions at coordinatively unsaturated metal sites can be strong and chemical in nature. We have used AIMD to remedy that but an alternate developed by some researchers is to create new FFs from QM data to study them [144]. While not yet available for catalysis, packages such as QuickFF [145] exist to facilitate construction of FFs for describing phenomena in MOFs from user-generated QM data.

In some cases, truncated cluster models are unable to accurately describe phenomena that are foundational to MOF catalyst function. For example, the MOF pore size and topology can play significant roles in driving reaction selectivity by stabilizing reaction intermediates and transition states. An example is C-H bond amination in the Mn-based MOF CPF-5, where confinement from the framework leads to rates faster than the homogeneous analog [146]. We have explored this in chapter-5 where a periodic model gives different rates that can partially be attributed to stabilization of the C_2H_4 species by linkers. For larger guest species whose size is comparable to pore-size these effects are expected to be more significant and a periodic model is recommended.

As elaborated previously MOFs exhibit different types of molecule transport that cannot all be modeled so straightforwardly. A future recommendation is to model the host-guest interactions that involves significant free energy barriers [147] for diffusion in smaller pore MOFs. Determining these barriers that are relevant to catalysis and incorporating them into a kinetic model can be non-straightforward. One strategy may be to assume that transport to the active site involves diffusion

along the pore surface and to model this phenomenon as an activated surface reaction (e.g., using transition state theory) [148]. It has been done for adsorption application in MOFs [147]. Such a strategy is well suited for microkinetic modeling, since the rate constants for diffusion and reaction will be on the same order of magnitude. A step towards that is in a recent publication with the DFT adsorption energies of ethene on various locations in the linkers in NU-1000 [149]. However, if diffusion and reaction occur over different time scales, kinetic Monte Carlo (kMC) may be useful. While there are no applications of kMC in catalysis in MOFs that we know of, kMC has recently been applied to zeolite catalysts [150, 151].

Appendices

Appendix A Appendix-A

1) Sample Gaussian-09 input file:

```
#p opt um06l/gen/auto geom=connectivity int=grid=ultrafine pseudo=read  
scf=(xqc,intrep,maxconventionalcycle=350) pop=(full,nbo,hirshfeld)
```

Title Card Required

0 4

S 5.06035836 1.32568064 -1.69510594

S 3.23621024 1.98823030 1.43699497

Mo 1.31125947 2.52806825 0.11580874

S 1.37515395 4.77852241 1.75843679

S -0.18531091 3.93478107 -1.13831450

S -0.08934131 1.63126528 1.75406617

S -1.60685840 0.94832220 -1.70647570

Mo -1.55684894 2.39738305 0.11318442

S -2.21730582 4.52240039 1.79505750

S -3.40507825 4.02339396 -1.16075839

S -3.43164475 1.61003780 1.41240242

S -5.04731362 0.86717087 -1.78938193

Mo 2.85873209 0.15012712 -0.02142846

S 3.48137098 -1.63375155 -1.50900307

Co -0.00325300 0.08947616 -0.09242330

Mo 1.59039174 -2.49278139 -0.38618931

S 0.09958150 -1.74388930 -1.96548033
S 0.20669487 -3.93640154 0.90995102
Mo -2.83710257 -0.16766378 -0.04781682
Mo -1.32191110 -2.63372976 -0.39837339
S -3.27660846 -1.97194313 -1.55632277
H -4.49692150 0.18928042 -2.82068738
H 5.74032189 0.16983017 -1.84869591
H 2.58308646 4.71675945 2.36316744
H -1.65321179 4.03510925 2.91866895
S 1.61662977 -1.02102553 1.48664328
S 1.50959911 1.08487128 -1.69941181
H -3.36826476 3.47738380 -2.39314877
S -4.90887978 -1.24033718 1.39656542
H -5.27246712 -2.26201395 0.58651597
H -5.87122038 -0.41658118 0.92970243
H -1.24833428 5.44808659 1.61192078
H 1.75656960 5.73985161 0.89297600
H 2.51248387 -3.74801847 2.67653871
H 4.29446281 1.05839001 -2.77361601
S 3.81285753 -3.83312751 2.33098207
H 3.51540908 -4.59727446 1.25482827
S -3.42100754 -4.22247946 2.34861139
H -2.11148482 -4.01474037 2.59499037
H -3.14174763 -4.83062196 1.17191230
S 5.02237921 -0.68816001 1.43417417
H 5.50841755 -1.66031507 0.62789142

S 3.00800666 4.29059225 -1.22735245
H 2.75478421 3.99126454 -2.51762075
H 4.25893857 3.77603534 -1.24100320
H 5.90324974 0.23829182 0.99861118
H -4.57966095 3.43444566 -0.83921534
H -5.97547957 -0.09321303 -1.60585599
S -1.48409347 -1.18931848 1.48007487
S -2.06193337 -4.76531899 -1.19608632
H -1.09079989 -5.55147109 -0.67183815
S 2.38055349 -4.63647963 -1.10447213
H 3.41551128 -4.30386039 -1.91110645

1 23 1.0 35 1.0

2 3 1.0 13 1.0

3 5 1.0 6 1.0 27 1.0

4 24 1.0 33 1.0

5 8 1.0

6 8 1.0

7 8 1.0 19 1.0

8 11 1.0

9 25 1.0 32 1.0

10 28 1.0 47 1.0

11 19 1.0

12 22 1.0 48 1.0

13 14 1.0 26 1.0 27 1.0

14 16 1.0

15

16 17 1.0 18 1.0 26 1.0 52 1.0

17 20 1.0

18 20 1.0

19 21 1.0 49 1.0

20 21 1.0 49 1.0 50 1.0

21

22

23

24

25

26

27

28

29 30 1.0 31 1.0

30

31

32

33

34 36 1.0

35

36 37 1.0

37

38 39 1.0 40 1.0

39

40

41 42 1.0 46 1.0

42

43 44 1.0 45 1.0

44

45

46

47

48

49

50 51 1.0

51

52 53 1.0

53

@path/H.gbs

@path/S.gbs

@path/Co.gbs

@path/Mo.gbs

2) Sample CP2K Geometry Optimization input file:

&GLOBAL

```
PRINT_LEVEL MEDIUM
PROJECT_NAME info-GEO-XXX
RUN_TYPE GEO_OPT
&END GLOBAL
&MOTION
&GEO_OPT
TYPE MINIMIZATION
OPTIMIZER BFGS
MAX_ITER 2000
MAX_DR 1.0000000000000000E-03
MAX_FORCE 1.0000000000000000E-04
RMS_DR 1.0000000000000000E-03
RMS_FORCE 1.0000000000000000E-04
STEP_START_VAL 0
&BFGS
TRUST_RADIUS 1.0000000000000001E-01
&END BFGS
&END GEO_OPT
&END MOTION
&FORCE_EVAL
METHOD QS
STRESS_TENSOR NONE
&DFT
BASIS_SET_FILE_NAME BASIS_file
POTENTIAL_FILE_NAME POTENTIALS_file
UKS
```

```
MULTIPLICITY 1
CHARGE 0
&SCF
MAX_SCF 1000
EPS_SCF 9.999999999999995E-07
SCF_GUESS ATOMIC
&OT T
MINIMIZER CG
PRECONDITIONER FULL_ALL
ENERGY_GAP 0.001
&END OT
&OUTER_SCF T
EPS_SCF 1.000000000E-5
MAX_SCF 50
&END OUTER_SCF
&END SCF
&QS
EPS_DEFAULT 1.000000000000000E-10
METHOD GPW
&END QS
&MGRID
NGRIDS 4
CUTOFF 3.600000000000000E+02
REL_CUTOFF 6.000000000000000E+01
&END MGRID
&XC
```

```
DENSITY_CUTOFF 1.0000000000000000E-10
GRADIENT_CUTOFF 1.0000000000000000E-10
TAU_CUTOFF 1.0000000000000000E-10
&XC_FUNCTIONAL NO_SHORTCUT
&PBE T
&END PBE
&END XC_FUNCTIONAL
&VDW_POTENTIAL
POTENTIAL_TYPE PAIR_POTENTIAL
&PAIR_POTENTIAL
TYPE DFTD3
R_CUTOFF 10.0
PARAMETER_FILE_NAME dftd3.dat
REFERENCE_FUNCTIONAL PBE
CALCULATE_C9_TERM F
&END PAIR_POTENTIAL
&END VDW_POTENTIAL
&END XC
&END DFT
&SUBSYS
&CELL
A 39.89700 0.00000 0.00000
B 19.94850 34.55182 0.00000
C 0.00000 0.00000 16.63500
&END CELL
&TOPOLOGY
```

```
COORD_FILE_NAME Ni-c2h5.xyz
COORD_FILE_FORMAT XYZ
&END TOPOLOGY

      &KIND C
BASIS_SET DZVP-MOLOPT-SR-GTH-q4
POTENTIAL GTH-PBE-q4
&END KIND

&KIND H
BASIS_SET DZVP-MOLOPT-SR-GTH-q1
POTENTIAL GTH-PBE-q1
&END KIND

&KIND Ni
BASIS_SET DZVP-MOLOPT-SR-GTH-q18
POTENTIAL GTH-PBE-q18
&END KIND

&KIND O
BASIS_SET DZVP-MOLOPT-SR-GTH-q6
POTENTIAL GTH-PBE-q6
&END KIND

&KIND Zr
BASIS_SET DZVP-MOLOPT-SR-GTH-q12
POTENTIAL GTH-PBE-q12
&END KIND

&END SUBSYS

&PRINT
```

```
&FORCES ON
&END FORCES
&END PRINT
&END FORCE_EVAL
```

3)Sample CP2K Frequency calculation input file:

```
&GLOBAL
PRINT_LEVEL MEDIUM
PROJECT_NAME info-GEO-XXX
RUN_TYPE VIBRATIONAL_ANALYSIS
&END GLOBAL
&VIBRATIONAL_ANALYSIS
THERMOCHEMISTRY T
NPROC_REP 40
&END VIBRATIONAL_ANALYSIS
&MOTION
&CONSTRAINT
&FIXED_ATOMS
COMPONENTS_TO_FIX XYZ
LIST 1..557
&END FIXED_ATOMS
&END CONSTRAINT
&END MOTION
&FORCE_EVAL
METHOD QS
STRESS_TENSOR NONE
```



```
&DFT
BASIS_SET_FILE_NAME BASIS_file
POTENTIAL_FILE_NAME POTENTIALS_file
UKS
MULTIPLICITY 1
CHARGE 0
&SCF
MAX_SCF 1000
EPS_SCF 9.999999999999995E-07
SCF_GUESS ATOMIC
&OT T
MINIMIZER CG
PRECONDITIONER FULL_ALL
ENERGY_GAP 0.001
&END OT
&OUTER_SCF T
EPS_SCF 1.000000000E-5
MAX_SCF 50
&END OUTER_SCF
&END SCF
&QS
EPS_DEFAULT 1.000000000000000E-10
METHOD GPW
&END QS
&MGRID
NGRIDS 4
```

```
CUTOFF 3.6000000000000000E+02
REL_CUTOFF 6.0000000000000000E+01
&END MGRID
&XC
DENSITY_CUTOFF 1.0000000000000000E-10
GRADIENT_CUTOFF 1.0000000000000000E-10
TAU_CUTOFF 1.0000000000000000E-10
&XC_FUNCTIONAL NO_SHORTCUT
&PBE T
&END PBE
&END XC_FUNCTIONAL
&VDW_POTENTIAL
POTENTIAL_TYPE PAIR_POTENTIAL
&PAIR_POTENTIAL
TYPE DFTD3
R_CUTOFF 10.0
PARAMETER_FILE_NAME dftd3.dat
REFERENCE_FUNCTIONAL PBE
CALCULATE_C9_TERM F
&END PAIR_POTENTIAL
&END VDW_POTENTIAL
&END XC
&END DFT
&SUBSYS
&CELL
A 39.89700 0.00000 0.00000
```

```

B 19.94850 34.55182 0.00000
C 0.00000 0.00000 16.63500
MULTIPLE_UNIT_CELL 1 1 1
SYMMETRY MONOCLINIC_GAMMA_AB
&END CELL
&TOPOLOGY
COORD_FILE_NAME Ni-c2h5.xyz
COORD_FILE_FORMAT XYZ
&END TOPOLOGY

      &KIND C
BASIS_SET DZVP-MOLOPT-SR-GTH-q4
POTENTIAL GTH-PBE-q4
&END KIND
&KIND H
BASIS_SET DZVP-MOLOPT-SR-GTH-q1
POTENTIAL GTH-PBE-q1
&END KIND
&KIND Ni
BASIS_SET DZVP-MOLOPT-SR-GTH-q18
POTENTIAL GTH-PBE-q18
&END KIND
&KIND O
BASIS_SET DZVP-MOLOPT-SR-GTH-q6
POTENTIAL GTH-PBE-q6
&END KIND

```

```
&KIND Zr
BASIS.SET DZVP-MOLOPT-SR-GTH-q12
POTENTIAL GTH-PBE-q12
&END KIND
&END SUBSYS
&PRINT
&FORCES ON
&END FORCES
&END PRINT
&END FORCE_EVAL
```

4) Sample CP2K AIMD calculation input file:

```
&GLOBAL
PRINT_LEVEL MEDIUM
PROJECT_NAME info-GEO-XXX
RUN_TYPE MD
&MOTION
&CONSTRAINT
&FIXED_ATOMS
COMPONENTS_TO_FIX XYZ
LIST 1..557
&END FIXED_ATOMS
&END CONSTRAINT
&GEO_OPT
TYPE MINIMIZATION
OPTIMIZER BFGS
```

```
MAX_ITER 2000
MAX_DR 1.0000000000000000E-03
MAX_FORCE 1.0000000000000000E-04
RMS_DR 1.0000000000000000E-03
RMS_FORCE 1.0000000000000000E-04
STEP_START_VAL 0
&BFGS
TRUST_RADIUS 1.0000000000000001E-01
&END BFGS
&END GEO_OPT
&MD
ENSEMBLE NVT
TEMPERATURE [K] 300
TIMESTEP [fs] 1
STEPS 1000
&THERMOSTAT
REGION GLOBAL
TYPE NOSE
&END THERMOSTAT
&END MD
&PRINT
&TRAJECTORY
&EACH
MD 1
&END EACH
&END TRAJECTORY
```

```
&VELOCITIES OFF
&END VELOCITIES
&FORCES OFF
&END FORCES
&RESTART_HISTORY
&EACH
MD 100
&END EACH
&END RESTART_HISTORY
&RESTART
BACKUP_COPIES 3
&EACH
MD 1
&END EACH
&END RESTART
&END PRINT
&END MOTION
&FORCE_EVAL
METHOD QS
STRESS_TENSOR NONE
&DFT
BASIS_SET_FILE_NAME BASIS_file
POTENTIAL_FILE_NAME POTENTIALS_file
UKS
MULTIPLICITY 1
CHARGE 0
```

```
&SCF
MAX_SCF 1000
EPS_SCF 9.999999999999995E-07
SCF_GUESS ATOMIC
&OT T
MINIMIZER CG
PRECONDITIONER FULL_ALL
ENERGY_GAP 0.001
&END OT
&OUTER_SCF T
EPS_SCF 1.000000000E-5
MAX_SCF 50
&END OUTER_SCF
&END SCF
&QS
EPS_DEFAULT 1.000000000000000E-10
METHOD GPW
&END QS
&MGRID
NGRIDS 4
CUTOFF 3.600000000000000E+02
REL_CUTOFF 6.000000000000000E+01
&END MGRID
&XC
DENSITY_CUTOFF 1.000000000000000E-10
GRADIENT_CUTOFF 1.000000000000000E-10
```

```
TAU_CUTOFF 1.0000000000000000E-10
&XC_FUNCTIONAL NO_SHORTCUT
&PBE T
&END PBE
&END XC_FUNCTIONAL
&VDW_POTENTIAL
POTENTIAL_TYPE PAIR_POTENTIAL
&PAIR_POTENTIAL
TYPE DFTD3
R_CUTOFF 10.0
PARAMETER_FILE_NAME dftd3.dat
REFERENCE_FUNCTIONAL PBE
CALCULATE_C9_TERM F
&END PAIR_POTENTIAL
&END VDW_POTENTIAL
&END XC
&END DFT
&SUBSYS
&CELL
A 39.89700 0.00000 0.00000
B 19.94850 34.55182 0.00000
C 0.00000 0.00000 16.63500
MULTIPLE_UNIT_CELL 1 1 1
SYMMETRY MONOCLINIC_GAMMA_AB
&END CELL
&TOPOLOGY
```



```
COORD_FILE_NAME Ni-c2h5.xyz
COORD_FILE_FORMAT XYZ
&END TOPOLOGY

      &KIND C
BASIS_SET DZVP-MOLOPT-SR-GTH-q4
POTENTIAL GTH-PBE-q4
&END KIND

&KIND H
BASIS_SET DZVP-MOLOPT-SR-GTH-q1
POTENTIAL GTH-PBE-q1
&END KIND

&KIND Ni
BASIS_SET DZVP-MOLOPT-SR-GTH-q18
POTENTIAL GTH-PBE-q18
&END KIND

&KIND O
BASIS_SET DZVP-MOLOPT-SR-GTH-q6
POTENTIAL GTH-PBE-q6
&END KIND

&KIND Zr
BASIS_SET DZVP-MOLOPT-SR-GTH-q12
POTENTIAL GTH-PBE-q12
&END KIND

&END SUBSYS

&PRINT
```

```
&FORCES ON
&END FORCES
&END PRINT
&END FORCE_EVAL
```

5)Sample RASPA Input file:

```
SimulationType MonteCarlo
NumberOfCycles 1500000000
NumberOfInitializationCycles 5000000
PrintEvery 1000000
Forcefield GenericMOFs
CutOff 12.8
Framework 0
FrameworkName Ni-h-c2h4-NU-1000
UnitCells 1 1 2
HeliumVoidFraction 0.801688
ExternalTemperature 298
ExternalPressure 1e5
Component 0 MoleculeName ethene-t
MoleculeDefinition TraPPE
TranslationProbability 1.0
RotationProbability 1.0
ReinsertionProbability 1.0
SwapProbability 1.0
CreateNumberOfMolecules 0
```

6)Sample Microkinetic Modeling MKMCXX input file:

Input for oligomerization of ethene with Ni-NU-1000

&compounds

Gas Species

format: NAME; isSite? ; starting concentration ; TDRC?

C2H4; 0; 1.0; 1

C4H8; 0; 0.0; 1

Adsorbates

format: NAME; isSite? ; starting concentration; TDRC?

c2h5; 1; 1.0

c2h5_c2h4; 1; 0.0; 1

c4h9; 1; 0.0; 1

h_c4h8; 1; 0.0; 1

h; 1; 0.0; 1

h_c2h4; 1; 0.0; 1

&reactions

adsorptions / desorptions

Hertz-Knudsen (HK); NAMEs; Surface Area (Ionic radius); gas mass; Rotational

#temperature; Symmetry number; sticking coefficient; desorption energy (ZPE)(J);DRC?

m² amu K sigma sticking J/mol

HK; {C2H4} + {c2h5} = {c2h5_c2h4}; 3.0895E-19; 28.05; 6.98; 4; 1.0000E+00;

6.2800E+04; 1

HK; {C2H4} + h = h_c2h4; 3.0895E-19; 28.05; 6.98; 4; 1.0000E+00; 1.6499E+05; 1
HK; {C4H8} + h = {h_c4h8}; 3.0895E-19; 56.10; 1.11; 1; 1.0000E+00; 3.4961E+04; 1

Surface reactions # Arrhenius (AR); NAMEs; forward pre-exponential; re-
verse pre-exponential;

#forward activation barrier(J); reverse activation barrier(J); DRC?

pre-exponential and activation barriers fitted using TAMKin

vf vb Eaf Eab

AR; {c2h5_c2h4} = {c4h9} ; 6.477518E+12; 4.574197E+12; 4.9546E+04; 1.0305E+05
; 1

AR; {c4h9} = {h_c4h8} ; 1.128640E+13; 3.563245E+13; 2.9031E+04; 1.0373E+04 ;
1

AR; {h_c2h4} = {c2h5} ; 5.130269E+13; 8.730372E+13; 2.9550E+04; 6.3323E+04 ;
1

&settings

TYPE = SEQUENCERUN

PRESSURE = 1

#REAGENTS need to be specified for ORDERS

REAGENTS = C2H4

#KEYCOMPONENTS need to be specified for ORDERS, EACT, DRC and TDRC

KEYCOMPONENTS = C4H8

#Calculates the reaction orders in the reagents (Default = 0)

ORDERS = 1

#Calculates the apparent activation energy (Default = 0)

EACT = 1

#Calculates the degree of rate control (Default = 0)

```
DRC = 1
#Calculates the thermodynamic degree of rate control (Default = 0)
TDRC = 1
#Enables debug messages. Also produces some data on relative derivatives (dydt/y)
to check for convergence (Default = 0)
DEBUG = 1
MAKEPLOTS = 0
GNUPLOT = 1
&runs
# Temp; Time; AbsTol; RelTol
298; 1e8; 1e-12; 1e-12
323; 1e8; 1e-12; 1e-12
348; 1e8; 1e-12; 1e-12
373; 1e8; 1e-12; 1e-12
398; 1e8; 1e-12; 1e-12
423; 1e8; 1e-12; 1e-12
448; 1e8; 1e-12; 1e-12
473; 1e8; 1e-12; 1e-12
```

Bibliography

- [1] Dharik S. Mallapragada, Gang Duan, and Rakesh Agrawal. From shale gas to renewable energy based transportation solutions. *Energy Policy*, 67:499–507, 2014.
- [2] Rob Gardner. The outlook for energy: A view to 2040. *2015 Engineering Deans Institute, EDI 2015 - Annual Conference*, 2015.
- [3] David A. Wood, Chikezie Nwaoha, and Brian F. Towler. Gas-to-liquids (GTL): A review of an industry offering several routes for monetizing natural gas. *Journal of Natural Gas Science and Engineering*, 9:196–208, 2012.
- [4] Victoria M. Ehlinger, Kerron J. Gabriel, Mohamed M.B. Noureldin, and Mahmoud M. El-Halwagi. Process design and integration of shale gas to methanol. *ACS Sustainable Chemistry and Engineering*, 2(1):30–37, 2014.
- [5] Chang He and Fengqi You. Shale gas processing integrated with ethylene production: Novel process designs, exergy analysis, and techno-economic analysis. *Industrial and Engineering Chemistry Research*, 53(28):11442–11459, 2014.
- [6] Sean E DeRosa. Impact of Natural Gas and Natural Gas Liquids on Chemical Manufacturing in the United States, 2016.
- [7] Lutz.B. New age gas-to-liquids processing, Nov 2001.
- [8] Taufik Ridha, Yiru Li, Emre Gener, Jeffrey J. Siirola, Jeffrey T. Miller, Fabio H. Ribeiro, and Rakesh Agrawal. Valorization of shale gas condensate to liquid hydrocarbons through catalytic dehydrogenation and oligomerization. *Processes*, 6(9):1–21, 2018.
- [9] Hans Schulz. Short history and present trends of Fischer-Tropsch synthesis. *Applied Catalysis A: General*, 186(1-2):3–12, 1999.
- [10] H. D. Gesser and N. R. Hunter. A review of C-1 conversion chemistry. *Catalysis Today*, 42(3):183–189, 1998.

- [11] Fredy Speiser, Pierre Braunstein, and Lucien Saussine. Catalytic ethylene dimerization and oligomerization: recent developments with nickel complexes containing P,N-chelating ligands. *Accounts of Chemical Research*, 38(10):784–793, 2005.
- [12] Bryan Reuben, Harold Wittcoff, and Harold Wittcoff. industrial chemistry, 1988.
- [13] Annie Finiels, Francois Fajula, and Vasile Hulea. Nickel-based solid catalysts for ethylene oligomerization-a review. *Catalysis Science and Technology*, 4(8):2412–2426, 2014.
- [14] Jesper J.H.B. Sattler, Javier Ruiz-Martinez, Eduardo Santillan-Jimenez, and Bert M. Weckhuysen. Catalytic dehydrogenation of light alkanes on metals and metal oxides. *Chemical Reviews*, 114(20):10613–10653, 2014.
- [15] Biplab Maji and Milan K. Barman. Recent Developments of Manganese Complexes for Catalytic Hydrogenation and Dehydrogenation Reactions. *Synthesis (Germany)*, 49(15):3377–3393, 2017.
- [16] Dong Yang and Bruce C. Gates. Catalysis by Metal Organic Frameworks: Perspective and Suggestions for Future Research. *ACS Catalysis*, 9(3):1779–1798, 2019.
- [17] Amarajothi Dhakshinamoorthy, Zhaohui Li, and Hermenegildo Garcia. Catalysis and photocatalysis by metal organic frameworks. *Chemical Society Reviews*, 47(22):8134–8172, 2018.
- [18] Jacklyn N. Hall and Praveen Bollini. Structure, characterization, and catalytic properties of open-metal sites in metal organic frameworks. *Reaction Chemistry and Engineering*, 4(2):207–222, 2019.
- [19] Qi Wang and Didier Astruc. State of the Art and Prospects in Metal-Organic Framework (MOF)-Based and MOF-Derived Nanocatalysis. *Chemical Reviews*, 120(2):1438–1511, 2020.
- [20] Anastasiya Bavykina, Nikita Kolobov, Il Son Khan, Jeremy A. Bau, Adrian Ramirez, and Jorge Gascon. Metal-Organic Frameworks in Heterogeneous Catalysis: Recent Progress, New Trends, and Future Perspectives. *Chemical Reviews*, 120(16):8468–8535, 2020.
- [21] Kenton E. Hicks, Andrew S. Rosen, Zoha H. Syed, Randall Q. Snurr, Omar K. Farha, and Justin M. Notestein. Zr6O8 node-catalyzed butene hydrogenation and isomerization in the metal-organic framework NU-1000. *ACS Catalysis*, 10(24):14959–14970, 2020.

- [22] Dong Yang, Manuel A. Ortuño, Varinia Bernales, Christopher J. Cramer, Laura Gagliardi, and Bruce C. Gates. Structure and Dynamics of Zr₆O₈ Metal-Organic Framework Node Surfaces Probed with Ethanol Dehydration as a Catalytic Test Reaction. *Journal of the American Chemical Society*, 140(10):3751–3759, 2018.
- [23] Zhigang Hu and Dan Zhao. Metal-organic frameworks with Lewis acidity: Synthesis, characterization, and catalytic applications. *CrystEngComm*, 19(29):4066–4081, 2017.
- [24] Varinia Bernales, Aaron B. League, Zhanyong Li, Neil M. Schweitzer, Aaron W. Peters, Rebecca K. Carlson, Joseph T. Hupp, Christopher J. Cramer, Omar K. Farha, and Laura Gagliardi. Computationally Guided Discovery of a Catalytic Cobalt-Decorated Metal-Organic Framework for Ethylene Dimerization. *Journal of Physical Chemistry C*, 120(41):23576–23583, 2016.
- [25] Jingyun Ye, Laura Gagliardi, Christopher J. Cramer, and Donald G. Truhlar. Single Ni atoms and Ni₄ clusters have similar catalytic activity for ethylene dimerization. *Journal of Catalysis*, 354:278–286, 2017.
- [26] Deependra M. Shakya, Otega A. Ejegbavwo, Thayalan Rajeshkumar, Sanjaya D. Senanayake, Amy J. Brandt, Sharfa Farzandh, Narayan Acharya, Amani M. Ebrahim, Anatoly I. Frenkel, Ning Rui, Gregory L. Tate, John R. Monnier, Konstantinos D. Vogiatzis, Natalia B. Shustova, and Donna A. Chen. Selective Catalytic Chemistry at Rhodium(II) Nodes in Bimetallic Metal-Organic Frameworks. *Angewandte Chemie - International Edition*, 58(46):16533–16537, 2019.
- [27] Maryam Samaniyan, Masoud Mirzaei, Ruhollah Khajavian, Hossein Eshtiagh-Hosseini, and Carsten Streb. Heterogeneous Catalysis by Polyoxometalates in Metal-Organic Frameworks. *ACS Catalysis*, 9(11):10174–10191, 2019.
- [28] Yingmu Zhang, Xinyu Yang, and Hong Cai Zhou. Synthesis of MOFs for heterogeneous catalysis via linker design. *Polyhedron*, 154:189–201, 2018.
- [29] Sayed Ali Akbar Razavi and Ali Morsali. Linker functionalized metal-organic frameworks. *Coordination Chemistry Reviews*, 399:213023, 2019.
- [30] Sukhendu Mandal, Srinivasan Natarajan, Prabu Mani, and Asha Pankajakshan. Post-Synthetic Modification of Metal-Organic Frameworks Toward Applications. *Advanced Functional Materials*, 31(4), 2021.
- [31] Timothy C. Wang, Nicolaas A. Vermeulen, In Soo Kim, Alex B.F. Martinson, J. Fraser Stoddart, Joseph T. Hupp, and Omar K. Farha. Scalable synthesis and post-modification of a mesoporous metal-organic framework called NU-1000. *Nature Protocols*, 11(1):149–162, 2016.

- [32] S. M.J. Rogge, A. Bavykina, J. Hajek, H. Garcia, A. I. Olivos-Suarez, A. Sepúlveda-Escribano, A. Vimont, G. Clet, P. Bazin, F. Kapteijn, M. Daturi, E. V. Ramos-Fernandez, F. X.I. Llabrés Xamena, V. Van Speybroeck, and J. Gascon. Metal-organic and covalent organic frameworks as single-site catalysts. *Chemical Society Reviews*, 46(11):3134–3184, 2017.
- [33] Gavin A. McCarver, Thayalan Rajeshkumar, and Konstantinos D. Vogiatzis. Computational catalysis for metal-organic frameworks: An overview. *Coordination Chemistry Reviews*, 436:213777, 2021.
- [34] Zhanyong Li, Aaron W. Peters, Varinia Bernales, Manuel A. Ortuño, Neil M. Schweitzer, Matthew R. Destefano, Leighanne C. Gallington, Ana E. Platero-Prats, Karena W. Chapman, Christopher J. Cramer, Laura Gagliardi, Joseph T. Hupp, and Omar K. Farha. Metal-Organic Framework Supported Cobalt Catalysts for the Oxidative Dehydrogenation of Propane at Low Temperature. *ACS Central Science*, 3(1):31–38, 2017.
- [35] Zhanyong Li, Neil M. Schweitzer, Aaron B. League, Varinia Bernales, Aaron W. Peters, Andrew Bean Getsoian, Timothy C. Wang, Jeffrey T. Miller, Aleksei Vjunov, John L. Fulton, Johannes A. Lercher, Christopher J. Cramer, Laura Gagliardi, Joseph T. Hupp, and Omar K. Farha. Sintering-Resistant Single-Site Nickel Catalyst Supported by Metal-Organic Framework. *Journal of the American Chemical Society*, 138(6):1977–1982, 2016.
- [36] Omar K. Farha, A. Özgür Yazaydin, Ibrahim Eryazici, Christos D. Malliakas, Brad G. Hauser, Mercouri G. Kanatzidis, Sonbinh T. Nguyen, Randall Q. Snurr, and Joseph T. Hupp. De novo synthesis of a metal-organic framework material featuring ultrahigh surface area and gas storage capacities. *Nature Chemistry*, 2(11):944–948, 2010.
- [37] Idan Hod, Pravas Deria, Wojciech Bury, Joseph E. Mondloch, Chung Wei Kung, Monica So, Matthew D. Sampson, Aaron W. Peters, Cliff P. Kubiak, Omar K. Farha, and Joseph T. Hupp. A porous proton-relaying metal-organic framework material that accelerates electrochemical hydrogen evolution. *Nature Communications*, 6:1–9, 2015.
- [38] Joseph E. Mondloch, Michael J. Katz, Nora Planas, David Semrouni, Laura Gagliardi, Joseph T. Hupp, and Omar K. Farha. Are Zr₆-based MOFs water stable? Linker hydrolysis vs. capillary-force-driven channel collapse. *Chemical Communications*, 50(64):8944–8946, 2014.
- [39] Timothy C. Wang, Nicolaas A. Vermeulen, In Soo Kim, Alex B.F. Martinson, J. Fraser Stoddart, Joseph T. Hupp, and Omar K. Farha. Scalable synthesis and post-modification of a mesoporous metal-organic framework called NU-1000. *Nature Protocols*, 11(1):149–162, 2016.

- [40] Timur Islamoglu, Subhadip Goswami, Zhanyong Li, Ashlee J. Howarth, Omar K. Farha, and Joseph T. Hupp. Postsynthetic Tuning of Metal-Organic Frameworks for Targeted Applications. *Accounts of Chemical Research*, 50(4):805–813, 2017.
- [41] Takaaki Ikuno, Jian Zheng, Aleksei Vjunov, Maricruz Sanchez-Sanchez, Manuel A. Ortuño, Dale R. Pahls, John L. Fulton, Donald M. Camaioni, Zhanyong Li, Debmalya Ray, B. Layla Mehdi, Nigel D. Browning, Omar K. Farha, Joseph T. Hupp, Christopher J. Cramer, Laura Gagliardi, and Johannes A. Lercher. Methane Oxidation to Methanol Catalyzed by Cu-Oxo Clusters Stabilized in NU-1000 Metal-Organic Framework. *Journal of the American Chemical Society*, 139(30):10294–10301, 2017.
- [42] Sai Puneet Desai, Jingyun Ye, Jian Zheng, Magali S. Ferrandon, Thomas E. Webber, Ana E. Platero-Prats, Jiaxin Duan, Paula Garcia-Holley, Donald M. Camaioni, Karena W. Chapman, Massimiliano Delferro, Omar K. Farha, John L. Fulton, Laura Gagliardi, Johannes A. Lercher, R. Lee Penn, Andreas Stein, and Connie C. Lu. Well-Defined Rhodium-Gallium Catalytic Sites in a Metal-Organic Framework: Promoter-Controlled Selectivity in Alkyne Semihydrogenation to E-Alkenes. *Journal of the American Chemical Society*, 140(45):15309–15318, 2018.
- [43] Sherzod T. Madrahimov, James R. Gallagher, Guanghui Zhang, Zachary Meinhart, Sergio J. Garibay, Massimiliano Delferro, Jeffrey T. Miller, Omar K. Farha, Joseph T. Hupp, and Sonbinh T. Nguyen. Gas-Phase Dimerization of Ethylene under Mild Conditions Catalyzed by MOF Materials Containing (bpy)NiII Complexes. *ACS Catalysis*, 5(11):6713–6718, 2015.
- [44] Hafeera Shabbir, Steven Pellizzeri, Magali Ferrandon, In Soo Kim, Nicolaas A. Vermeulen, Omar K. Farha, Massimiliano Delferro, Alex B.F. Martinson, and Rachel B. Getman. Influence of spin state and electron configuration on the active site and mechanism for catalytic hydrogenation on metal cation catalysts supported on NU-1000: insights from experiments and microkinetic modeling. *Catalysis Science and Technology*, 10(11):3594–3602, 2020.
- [45] Jingyun Ye, Laura Gagliardi, Christopher J. Cramer, and Donald G. Truhlar. Computational screening of MOF-supported transition metal catalysts for activity and selectivity in ethylene dimerization. *Journal of Catalysis*, 360:160–167, 2018.
- [46] Steven Pellizzeri, Melissa Barona, Varinia Bernales, Pere Miró, Peilin Liao, Laura Gagliardi, Randall Q. Snurr, and Rachel B. Getman. Catalytic descriptors and electronic properties of single-site catalysts for ethene dimerization to 1-butene. *Catalysis Today*, 2018.

- [47] R. O. Jones. Density functional theory: Its origins, rise to prominence, and future. *Rev. Mod. Phys.*, 87:897–923, Aug 2015.
- [48] Christopher J. Cramer and Donald G. Truhlar. Density functional theory for transition metals and transition metal chemistry. *Physical Chemistry Chemical Physics*, 11(46):10757–10816, 2009.
- [49] Wanyi Jiang, Nathan J. Deyonker, and Angela K. Wilson. Multireference character for 3d transition-metal-containing molecules. *Journal of Chemical Theory and Computation*, 8(2):460–468, 2012.
- [50] Soumen Ghosh, Pragya Verma, Christopher J. Cramer, Laura Gagliardi, and Donald G. Truhlar. Combining Wave Function Methods with Density Functional Theory for Excited States. *Chemical Reviews*, 118(15):7249–7292, 2018.
- [51] Tokmako, A. time dependent quantum mechanics and spectroscopy. <https://chem.libretexts.org/@go/page/107250>, 2020 (accessed December 17, 2021).
- [52] Christopher Campbell, Carlos A. Ferreiro-Rangel, Michael Fischer, José R.B. Gomes, and Miguel Jorge. A transferable model for adsorption in mofs with unsaturated metal sites. *Journal of Physical Chemistry C*, 121(1):441–458, 2017.
- [53] MJEAFrisch, Gary W Trucks, H Bernhard Schlegel, Gustavo E Scuseria, Michael A Robb, James R Cheeseman, Giovanni Scalmani, Vincenzo Barone, Benedetta Mennucci, GAeA Petersson, et al. Gaussian 09, revision c. 01, 2009.
- [54] Yan Zhao and Donald G. Truhlar. A new local density functional for main-group thermochemistry, transition metal bonding, thermochemical kinetics, and noncovalent interactions. *Journal of Chemical Physics*, 125(19), 2006.
- [55] Yan Zhao and Donald G. Truhlar. Density functionals with broad applicability in chemistry. *Accounts of Chemical Research*, 41(2):157–167, 2008.
- [56] John P. Perdew, Kieron Burke, and Matthias Ernzerhof. Generalized gradient approximation made simple [phys. rev. lett. 77, 3865 (1996)]. *Phys. Rev. Lett.*, 78:1396–1396, Feb 1997.
- [57] Florian Weigend and Reinhart Ahlrichs. Balanced basis sets of split valence, triple zeta valence and quadruple zeta valence quality for H to Rn: Design and assessment of accuracy. *Physical Chemistry Chemical Physics*, 7(18):3297–3305, 2005.
- [58] Florian Weigend. Accurate Coulomb-fitting basis sets for H to Rn. *Physical Chemistry Chemical Physics*, 8(9):1057–1065, 2006.

- [59] Xiaosong Li and Michael J. Frisch. Energy-represented direct inversion in the iterative subspace within a hybrid geometry optimization method. *Journal of Chemical Theory and Computation*, 2(3):835–839, 2006.
- [60] Thomas D. Kühne, Marcella Iannuzzi, Mauro Del Ben, Vladimir V. Rybkin, Patrick Seewald, Frederick Stein, Teodoro Laino, Rustam Z. Khaliullin, Ole Schütt, Florian Schiffmann, Dorothea Golze, Jan Wilhelm, Sergey Chulkov, Mohammad Hossein Bani-Hashemian, Valéry Weber, Urban Borštnik, Mathieu Taillefumier, Alice Shoshana Jakobovits, Alfio Lazzaro, Hans Pabst, Tiziano Müller, Robert Schade, Manuel Guidon, Samuel Andermatt, Nico Holmberg, Gregory K. Schenter, Anna Hehn, Augustin Bussy, Fabian Belleflamme, Gloria Tabacchi, Andreas Glöß, Michael Lass, Iain Bethune, Christopher J. Mundy, Christian Plessl, Matt Watkins, Joost VandeVondele, Matthias Krack, and Jürg Hutter. CP2K: An electronic structure and molecular dynamics software package -Quickstep: Efficient and accurate electronic structure calculations. *Journal of Chemical Physics*, 152(19), 2020.
- [61] Stefan Grimme, Jens Antony, Stephan Ehrlich, and Helge Krieg. A consistent and accurate ab initio parametrization of density functional dispersion correction (dft-d) for the 94 elements h-pu. *The Journal of Chemical Physics*, 132(15):154104, 2010.
- [62] S. Goedecker, M. Teter, and J. Hutter. Separable dual-space gaussian pseudopotentials. *Phys. Rev. B*, 54:1703–1710, Jul 1996.
- [63] An Ghysels, Toon Verstraelen, Karen Hemelsoet, Michel Waroquier, and Veronique Van Speybroeck. TAMkin: A versatile package for vibrational analysis and chemical kinetics. *Journal of Chemical Information and Modeling*, 50(9):1736–1750, 2010.
- [64] Raphael F. Ribeiro, Aleksandr V. Marenich, Christopher J. Cramer, and Donald G. Truhlar. Use of solution-phase vibrational frequencies in continuum models for the free energy of solvation. *Journal of Physical Chemistry B*, 115(49):14556–14562, 2011.
- [65] Bart A. De Moor, An Ghysels, Marie Françoise Reyniers, Veronique Van Speybroeck, Michel Waroquier, and Guy B. Marin. Normal mode analysis in zeolites: Toward an efficient calculation of adsorption entropies. *Journal of Chemical Theory and Computation*, 7(4):1090–1101, 2011.
- [66] I. M. Alecu, Jingjing Zheng, Yan Zhao, and Donald G. Truhlar. Computational thermochemistry: Scale factor databases and scale factors for vibrational frequencies obtained from electronic model chemistries. *Journal of Chemical Theory and Computation*, 6(9):2872–2887, 2010.

- [67] Manoj K. Kesharwani, Brina Brauer, and Jan M.L. Martin. Frequency and zero-point vibrational energy scale factors for double-hybrid density functionals (and other selected methods): Can anharmonic force fields be avoided? *Journal of Physical Chemistry A*, 119(9):1701–1714, 2015.
- [68] Collin D. Wick, Marcus G. Martin, and J. Ilja Siepmann. Transferable Potentials for Phase Equilibria. 4. United-Atom description of linear and branched alkenes and alkylbenzenes. *Journal of Physical Chemistry B*, 104(33):8008–8016, 2000.
- [69] Stephen L. Mayo, Barry D. Olafson, and William A. Goddard. DREIDING: A generic force field for molecular simulations. *Journal of Physical Chemistry*, 94(26):8897–8909, 1990.
- [70] W. M. Skid A. K. Rappe, C. J. Casewit, K. S. Colwell, W. A. Goddard III. UFF, a full periodic table force field for molecular mechanics and molecular dynamics simulations. *J. Journal of American Chemical Society*, 114:1002410035, 1992.
- [71] David Dubbeldam, Sofia Calero, Donald E. Ellis, and Randall Q. Snurr. RASPA: Molecular simulation software for adsorption and diffusion in flexible nanoporous materials. *Molecular Simulation*, 42(2):81–101, 2016.
- [72] Oleksii V. Gutov, Wojciech Bury, Diego A. Gomez-Gualdron, Vaiva Krungleviciute, David Fairen-Jimenez, Joseph E. Mondloch, Amy A. Sarjeant, Salih S. Al-Juaid, Randall Q. Snurr, Joseph T. Hupp, Taner Yildirim, and Omar K. Farha. Water-Stable Zirconium-Based Metal–Organic Framework Material with High-Surface Area and Gas-Storage Capacities. *Chemistry - A European Journal*, 20(39):12389–12393, 2014.
- [73] Haoyuan Chen and Randall Q. Snurr. Understanding the Loading Dependence of Adsorbate Diffusivities in Hierarchical Metal-Organic Frameworks. *Langmuir*, 36(5):1372–1378, 2020.
- [74] Ernesto Vargas L. and Randall Q. Snurr. Heterogeneous Diffusion of Alkanes in the Hierarchical Metal-Organic Framework NU-1000. *Langmuir*, 31(36):10056–10065, 2015.
- [75] Steve Plimpton. Fast parallel algorithms for short-range molecular dynamics. *Journal of Computational Physics*, 117(1):1–19, 1995.
- [76] William C. Swope, Hans C. Andersen, Peter H. Berens, and Kent R. Wilson. A computer simulation method for the calculation of equilibrium constants for the formation of physical clusters of molecules: Application to small water clusters. *The Journal of Chemical Physics*, 76(1):637–649, 1982.

- [77] William G. Hoover. Canonical dynamics: Equilibrium phase-space distributions. *Phys. Rev. A*, 31:1695–1697, Mar 1985.
- [78] R. Car and M. Parrinello. Unified Approach for Molecular Dynamics and Density-Functional Theory. *Physical Review Letters*, 55(22):2471–2474, nov 1985.
- [79] Mark E. Tuckerman. Ab initio molecular dynamics: Basic concepts, current trends and novel applications. *Journal of Physics Condensed Matter*, 14(50), 2002.
- [80] Mark A. Schroeder and Mark S. Wrighton. Pentacarbonyliron(0) Photocatalyzed Hydrogenation and Isomerization of Olefins. *Journal of the American Chemical Society*, 98(2):551–558, 1976.
- [81] Avik Halder, Sungsik Lee, Bing Yang, Michael J. Pellin, Stefan Vajda, Zhanyong Li, Ying Yang, Omar K. Farha, and Joseph T. Hupp. Structural reversibility of Cu doped NU-1000 MOFs under hydrogenation conditions. *Journal of Chemical Physics*, 152(8), 2020.
- [82] In Soo Kim, Sol Ahn, Nicolaas A. Vermeulen, Thomas E. Webber, Leighanne C. Gallington, Karena W. Chapman, R. Lee Penn, Joseph T. Hupp, Omar K. Farha, Justin M. Notestein, and Alex B.F. Martinson. The Synthesis Science of Targeted Vapor-Phase Metal-Organic Framework Postmodification. *Journal of the American Chemical Society*, 142(1):242–250, 2020.
- [83] Ivo A.W. Filot, Robin J.P. Broos, Jeaphianne P.M. Van Rijn, Gerardus J.H.A. Van Heugten, Rutger A. Van Santen, and Emiel J.M. Hensen. First-Principles-Based Microkinetics Simulations of Synthesis Gas Conversion on a Stepped Rhodium Surface. *ACS Catalysis*, 5(9):5453–5467, 2015.
- [84] Ivo A.W. Filot, Rutger A. Van Santen, and Emiel J.M. Hensen. The optimally performing Fischer-Tropsch catalyst. *Angewandte Chemie - International Edition*, 53(47):12746–12750, 2014.
- [85] I.A.W Filot. *Introduction to Microkinetic Modeling*. Technische Universiteit Eindhoven, 2018.
- [86] M. Fournier MT Pope, Y. Jeannin. *Heteropoly and Isopoly oxometalates*. 0172-7966. Springer Berlin Heidelberg, 1983.
- [87] James Keggin. Structure of the Crystals of 12-Phosphotungstic Acid. *Nature*, 132:351–351, 1933.
- [88] B. Dawson. The structure of the 9(18)-heteropoly anion in potassium 9(18)-tungstophosphate, $K_6(P_2W_{18}O_{62}) \cdot 14H_2O$. *Acta Crystallographica*, 6(2):113–126, 1953.

- [89] J. Stuart Anderson. Constitution of the poly-acids [7]. *Nature*, 140(3550):850, 1937.
- [90] T. H. Evans Jr. THE CRYSTAL STRUCTURES OF AMMONIUM AND POTASSIUM MOLYBDOTELLURATES. *Journal of the American Chemical Society*, 0(3):0–1, 1948.
- [91] Ivan V. Kozhevnikov. Catalysis by heteropoly acids and multicomponent polyoxometalates in liquid-phase reactions. *Chemical Reviews*, 98(1):171–198, 1998.
- [92] De Liang Long, Ryo Tsunashima, and Leroy Cronin. Polyoxometalates: Building blocks for functional nanoscale systems. *Angewandte Chemie - International Edition*, 49(10):1736–1758, 2010.
- [93] Leanne G. Bloor, Renata Solarska, Krzysztof Bienkowski, Pawel J. Kulesza, Jan Augustynski, Mark D. Symes, and Leroy Cronin. Solar-driven water oxidation and decoupled hydrogen production mediated by an electron-coupled-proton buffer. *Journal of the American Chemical Society*, 138(21):6707–6710, 2016.
- [94] Ning Li, Jiang Liu, Bao-Xia Dong, and Ya-Qian Lan. Polyoxometalate-Based Compounds for Photo- and Electrocatalytic Applications. *Angewandte Chemie*, 132(47):20963–20977, 2020.
- [95] Hongjin Lv, Yurii V. Geletii, Chongchao Zhao, James W. Vickers, Guibo Zhu, Zhen Luo, Jie Song, Tianquan Lian, Djameladdin G. Musaev, and Craig L. Hill. Polyoxometalate water oxidation catalysts and the production of green fuel. *Chemical Society Reviews*, 41(22):7572–7589, 2012.
- [96] Li Hua, Yunxiang Qiao, Huan Li, Bo Feng, Zhenyan Pan, Yinyin Yu, Wenwen Zhu, and Zhenshan Hou. Epoxidation of olefins with hydrogen peroxide catalyzed by a reusable lacunary-type phosphotungstate catalyst. *Science China Chemistry*, 54(5):769–773, 2011.
- [97] Zhuohong Zhou, Guoyong Dai, Shi Ru, Han Yu, and Yongge Wei. Highly selective and efficient olefin epoxidation with pure inorganic-ligand supported iron catalysts. *Dalton Transactions*, 48(37):14201–14205, 2019.
- [98] Bin Zhang, Hiroyuki Asakura, and Ning Yan. Atomically Dispersed Rhodium on Self-Assembled Phosphotungstic Acid: Structural Features and Catalytic CO Oxidation Properties. *Industrial and Engineering Chemistry Research*, 56(13):3578–3587, 2017.
- [99] Dylan J. Thompson, Yang Zhang, and Tong Ren. Polyoxometalate [-SiW₁₀O₃₄(H₂O)₂]₄- on MCM-41 as catalysts for sulfide oxygenation with hydrogen peroxide. *Journal of Molecular Catalysis A: Chemical*, 392:188–193, 2014.

- [100] Razieh Fazaeli, Hamid Aliyan, Mohammad Ali Ahmadi, and Saeedeh Hashemian. Host (aluminum incorporated mesocellulose silica foam (Al-MCF))-guest (tungsten polyoxometalate) nanocomposite material: An efficient and reusable catalyst for selective oxidation of sulfides to sulfoxides and sulfones. *Catalysis Communications*, 29:48–52, 2012.
- [101] R. Frenzel, D. Morales, G. Romanelli, G. Sathicq, M. Blanco, and L. Pizzio. Synthesis, characterization and catalytic evaluation of H3PW12O40 included in acrylic acid/acrylamide polymer for the selective oxidation of sulfides. *Journal of Molecular Catalysis A: Chemical*, 420:124–133, 2016.
- [102] Haralampos N. Miras, Laia Vilà-Nadal, and Leroy Cronin. Polyoxometalate based open-frameworks (POM-OFs). *Chemical Society Reviews*, 43(16):5679–5699, 2014.
- [103] Heping Ma, Bailing Liu, Bin Li, Liming Zhang, Yang Guang Li, Hua Qiao Tan, Hong Ying Zang, and Guangshan Zhu. Cationic Covalent Organic Frameworks: A Simple Platform of Anionic Exchange for Porosity Tuning and Proton Conduction. *Journal of the American Chemical Society*, 138(18):5897–5903, 2016.
- [104] C. Férey, C. Mellot-Draznieks, C. Serre, F. Millange, J. Dutour, S. Surblé, and I. Margiolaki. Chemistry: A chromium terephthalate-based solid with unusually large pore volumes and surface area. *Science*, 309(5743):2040–2042, 2005.
- [105] Dong Ying Du, Jun Shen Qin, Shun Li Li, Zhong Min Su, and Ya Qian Lan. Recent advances in porous polyoxometalate-based metal-organic framework materials. *Chemical Society Reviews*, 43(13):4615–4632, 2014.
- [106] Sol Ahn, Scott L. Nauert, Cassandra T. Buru, Martino Rimoldi, Hyeju Choi, Neil M. Schweitzer, Joseph T. Hupp, Omar K. Farha, and Justin M. Notestine. Pushing the Limits on Metal-Organic Frameworks as a Catalyst Support: NU-1000 Supported Tungsten Catalysts for *o*-Xylene Isomerization and Disproportionation. *Journal of the American Chemical Society*, 140(27):8535–8543, 2018.
- [107] Seiji Ogo, Takahiro Kishima, Takeshi Yatabe, Keishi Miyazawa, Ryunosuke Yamasaki, Takahiro Matsumoto, Tatsuya Ando, Mitsuhiro Kikkawa, Miho Isegawa, Ki Seok Yoon, and Shinya Hayami. [NiFe], [FeFe], and [Fe] hydrogenase models from isomers. *Science Advances*, 6(24):1–11, 2020.
- [108] R. David Britt, Guodong Rao, and Lizhi Tao. Bioassembly of complex iron–sulfur enzymes: hydrogenases and nitrogenases, 2020.
- [109] Alex McSkimming and Daniel L.M. Suess. Dinitrogen binding and activation at a molybdenum–iron–sulfur cluster. *Nature Chemistry*, 13(7):666–670, 2021.

- [110] Jing Lin Zuo, Hong Cai Zhou, and R. H. Holm. Vanadium-iron-sulfur clusters containing the cubane-type [VFE₃S₄] core unit: Synthesis of a cluster with the topology of the PN cluster of nitrogenase. *Inorganic Chemistry*, 42(15):4624–4631, 2003.
- [111] Sean F. Jordan, Ioannis Ioannou, Hanadi Rammu, Aaron Halpern, Lara K. Bogart, Minkoo Ahn, Rafaela Vasiliadou, John Christodoulou, Amandine Maréchal, and Nick Lane. Spontaneous assembly of redox-active iron-sulfur clusters at low concentrations of cysteine. *Nature Communications*, 12(1):1–14, 2021.
- [112] Justin T. Henthorn, Renee J. Arias, Sergey Koroidov, Thomas Kroll, Dimosthenis Sokaras, Uwe Bergmann, Douglas C. Rees, and Serena DeBeer. Localized Electronic Structure of Nitrogenase FeMoco Revealed by Selenium K-Edge High Resolution X-ray Absorption Spectroscopy. *Journal of the American Chemical Society*, 141(34):13676–13688, 2019.
- [113] Qin Liu, Dawn Duan, Hafeera Shabbir, Zhinhingyu Chen, Wentuan Bi, Z. Lu, N. Schweitzer, Alayoglu S, Subhadip Goswami, Rachel B. Getman, Karena Chapman, and Joseph T. Hupp. Presentation of Gas-phase-reactant-accessible Single-rhodium-atom Catalysts for CO Oxidation, via MOF Confinement of an Anderson Polyoxometalate. *J Mat Chemistry A (submitted under review)*, 2022.
- [114] Qin Liu, Hafeera Shabbir, Dawn Duan, , Zhinhingyu Chen, Wentuan Bi, R Liu, Karena Chapman, A. B. F. Martinson, and Joseph T. Hupp. Polysulfidometalate clusters confined in metal-organic framework for enhanced electrochemical hydrogen evolution. *in-preparation*, 2022.
- [115] Amir Blazevic and Annette Rompel. The Anderson-Evans polyoxometalate: From inorganic building blocks via hybrid organic-inorganic structures to tomorrow's "Bio-POM". *Coordination Chemistry Reviews*, 307:42–64, 2016.
- [116] Hojin Jeong, Geonhee Lee, Beom Sik Kim, Junemin Bae, Jeong Woo Han, and Hyunjoo Lee. Fully Dispersed Rh Ensemble Catalyst to Enhance Low-Temperature Activity. *Journal of the American Chemical Society*, 140(30):9558–9565, 2018.
- [117] Max J Hülsey, Bin Zhang, Zhirui Ma, Hiroyuki Asakura, Tsunehiro Tanaka, Peng Zhang, Zili Wu, Ning Yan, David A Do, and Wei Chen. single-atom catalysts for CO oxidation. *Nature Communications*, 2019.
- [118] Hyunho Noh, Chung Wei Kung, Ken Ichi Otake, Aaron W. Peters, Zhanyong Li, Yijun Liao, Xinyi Gong, Omar K. Farha, and Joseph T. Hupp. Redox-Mediator-Assisted Electrocatalytic Hydrogen Evolution from Water by a Molybdenum Sulfide-Functionalized Metal-Organic Framework. *ACS Catalysis*, 8(10):9848–9858, 2018.

- [119] Ana E. Platero-Prats, Andreas Mavrandonakis, Leighanne C. Gallington, Yangyang Liu, Joseph T. Hupp, Omar K. Farha, Christopher J. Cramer, and Karena W. Chapman. Structural Transitions of the Metal-Oxide Nodes within Metal-Organic Frameworks: On the Local Structures of NU-1000 and UiO-66. *Journal of the American Chemical Society*, 138(12):4178–4185, 2016.
- [120] C L Farrow, P Juhas, J W Liu, D Bryndin, E S Božin, J Bloch, Th Proffen, and S J L Billinge. PDFfit2 and PDFgui: computer programs for studying nanostructure in crystals. *Journal of Physics: Condensed Matter*, 19(33):335219, jul 2007.
- [121] R. R. Cavanagh and J. T. Yates. Site distribution studies of Rh supported on Al₂O₃ - An infrared study of chemisorbed CO. *The Journal of Chemical Physics*, 74(7):4150–4155, 1981.
- [122] John T. Yates, T. Michael Duncan, and Robert W. Vaughan. Infrared spectroscopic study of activated surface processes: CO chemisorption on supported Rh. *Journal of Chemical Physics*, 71(10):3908–3915, 1979.
- [123] John C. Matsubu, Vanessa N. Yang, and Phillip Christopher. Isolated metal active site concentration and stability control catalytic CO₂ reduction selectivity. *Journal of the American Chemical Society*, 137(8):3076–3084, 2015.
- [124] Hafeera Shabbir. Si for comosx@nu-1000. https://github.com/getman-research-group/SI_CoMo6SX.
- [125] Eric Walker, Salai Cheettu Ammal, Gabriel A. Terejanu, and Andreas Heyden. Uncertainty Quantification Framework Applied to the Water-Gas Shift Reaction over Pt-Based Catalysts. *Journal of Physical Chemistry C*, 120(19):10328–10339, 2016.
- [126] Charles T. Campbell and Jason R.V. Sellers. The entropies of adsorbed molecules. *Journal of the American Chemical Society*, 134(43):18109–18115, 2012.
- [127] Charles Fricke, Biplab Rajbanshi, Eric A. Walker, Gabriel Terejanu, and Andreas Heyden. Propane Dehydrogenation on Platinum Catalysts: Identifying the Active Sites through Bayesian Analysis. *ACS Catalysis*, 12(4):2487–2498, 2022.
- [128] Wenbo Xie, Jiayan Xu, Yunxuan Ding, and P. Hu. Quantitative Studies of the Key Aspects in Selective Acetylene Hydrogenation on Pd(111) by Microkinetic Modeling with Coverage Effects and Molecular Dynamics. *ACS Catalysis*, 11(7):4094–4106, 2021.

- [129] Thomas M. Osborn Popp, Ariel Z. Plantz, Omar M. Yaghi, and Jeffrey A. Reimer. Precise Control of Molecular Self-Diffusion in Isoreticular and Multivariate Metal-Organic Frameworks. *ChemPhysChem*, 21(1):32–35, 2020.
- [130] Juergen Caro. Diffusion coefficients in nanoporous solids derived from membrane permeation measurements. *Adsorption*, 27(3):283–293, 2020.
- [131] Olexandra Zybalyo, Osama Shekhah, Hui Wang, Maxim Tafipolsky, Rochus Schmid, Diethelm Johannsmann, and Christof Wöll. A novel method to measure diffusion coefficients in porous metal-organic frameworks. *Physical Chemistry Chemical Physics*, 12(28):8092–8097, 2010.
- [132] Qingyuan Yang, Hervé Jobic, Fabrice Salles, Daniil Kolokolov, Vincent Guillerm, Christian Serre, and Guillaume Maurin. Probing the dynamics of CO₂ and CH₄ within the porous zirconium terephthalate UiO-66(Zr): A synergic combination of neutron scattering measurements and molecular simulations. *Chemistry - A European Journal*, 17(32):8882–8889, 2011.
- [133] Jacob J. Wardzala, Jonathan P. Ruffley, Isabella Goodenough, Allie M. Schmidt, Priyanka B. Shukla, Xin Wei, Abhishek Bagusetty, Mattheus De Souza, Prasenjit Das, Dorian J. Thompson, Christopher J. Karwacki, Christopher E. Wilmer, Eric Borguet, Nathaniel L. Rosi, and J. Karl Johnson. Modeling of Diffusion of Acetone in UiO-66. *Journal of Physical Chemistry C*, 124(52):28469–28478, 2020.
- [134] V Guillerm, C Serre, C L Zhong, and G Maurin. *Combination of Experimental and Modeling Tools*, 2014.
- [135] Karina Hemmer, Mirza Cokoja, and Roland A. Fischer. Exploitation of Intrinsic Confinement Effects of MOFs in Catalysis. *ChemCatChem*, 13(7):1683–1691, 2021.
- [136] Hafeera Shabbir. Mkm-custom-kads. <https://github.com/getman-research-group/microkinetic-modeling-code>.
- [137] Marcin Rybicki and Joachim Sauer. Ab Initio Prediction of Proton Exchange Barriers for Alkanes at Brønsted Sites of Zeolite H-MFI. *Journal of the American Chemical Society*, 140(51):18151–18161, 2018.
- [138] Albert Bruix, Johannes T. Margraf, Mie Andersen, and Karsten Reuter. First-principles-based multiscale modelling of heterogeneous catalysis. *Nature Catalysis*, 2(8):659–670, 2019.
- [139] Hafeera Shabbir, Stephen P. Vicchio, Paul Meza-Morales, and Rachel B. Getman. Role of Molecular Simulations in the Design of Metal-Organic Frameworks

- for Gas-Phase Thermocatalysis: A Perspective. *Journal of Physical Chemistry C*, 126(14):6111–6118, 2022.
- [140] Jeremy N. Harvey. Understanding the kinetics of spin-forbidden chemical reactions. *Physical Chemistry Chemical Physics*, 9(3):331–343, 2007.
- [141] Carlo Alberto Gaggioli, Leonardo Belpassi, Francesco Tarantelli, Jeremy N. Harvey, and Paola Belanzoni. Spin-Forbidden Reactions: Adiabatic Transition States Using Spin-Orbit Coupled Density Functional Theory. *Chemistry - A European Journal*, 24(20):5006–5015, 2018.
- [142] Bo Yang, Laura Gagliardi, and Donald G. Truhlar. Transition states of spin-forbidden reactions. *Physical Chemistry Chemical Physics*, 20(6):4129–4136, 2018.
- [143] Kai Cui and J. R. Schmidt. Enabling Efficient and Accurate Computational Studies of MOF Reactivity via QM/MM and QM/QM Methods. *Journal of Physical Chemistry C*, 124(19):10550–10560, 2020.
- [144] Allison L. Dzubak, Li Chiang Lin, Jihan Kim, Joseph A. Swisher, Roberta Poloni, Sergey N. Maximoff, Berend Smit, and Laura Gagliardi. Ab initio carbon capture in open-site metal-organic frameworks. *Nature Chemistry*, 4(10):810–816, 2012.
- [145] Louis Vanduyfhuys, Steven Vandenbrande, Toon Verstraelen, Rochus Schmid, Michel Waroquier, and Veronique Van Speybroeck. QuickFF: A program for a quick and easy derivation of force fields for metal-organic frameworks from ab initio input. *Journal of Computational Chemistry*, 36(13):1015–1027, 2015.
- [146] Le Wang, Douglas W. Agnew, Xiao Yu, Joshua S. Figueroa, and Seth M. Cohen. A Metal-Organic Framework with Exceptional Activity for C-H Bond Amination. *Angewandte Chemie - International Edition*, 57(2):511–515, 2018.
- [147] Mayank Agrawal, Salah E. Boulfelfel, Dorina F. Sava Gallis, Jeffery A. Greathouse, and David S. Sholl. Determining Diffusion Coefficients of Chemical Warfare Agents in Metal-Organic Frameworks. *Journal of Physical Chemistry Letters*, 10(24):7823–7830, 2019.
- [148] Felipe Polo-Garzon, Joseph K. Scott, and David A. Bruce. Microkinetic model for the dry reforming of methane on Rh doped pyrochlore catalysts. *Journal of Catalysis*, 340:196–204, 2016.
- [149] Ana E. Platero-Prats, Andreas Mavrandonakis, Jian Liu, Zhihengyu Chen, Zhijie Chen, Zhanyong Li, Andrey A. Yakovenko, Leighanne C. Gallington, Joseph T. Hupp, Omar K. Farha, Christopher J. Cramer, and Karena W.

- Chapman. The Molecular Path Approaching the Active Site in Catalytic Metal–Organic Frameworks. *Journal of the American Chemical Society*, 143(48):20090–20094, 2021.
- [150] Mykela DeLuca and David D. Hibbitts. Prediction of C6–C12 Interconversion Rates Using Novel Zeolite-specific Kinetic Monte Carlo Simulation Methods. *ChemRxiv*, 1, 2019.
- [151] Mykela Deluca, Pavlo Kravchenko, Alexander Hoffman, and David Hibbitts. Mechanism and Kinetics of Methylating C6-C12 Methylbenzenes with Methanol and Dimethyl Ether in H-MFI Zeolites. *ACS Catalysis*, 9(7):6444–6460, 2019.